Kinetic Freeze-Out Properties from Transverse Momentum Spectra of Pions in High Energy Proton-Proton Collisions

Li-Li Li and Fu-Hu Liu *

Institute of Theoretical Physics & State Key Laboratory of Quantum Optics and Quantum Optics Devices, Shanxi University, Taiyuan 030006, China; shanxi_lll@163.com
* Correspondence: fuhuliu@163.com or fuhuliu@sxu.edu.cn

check for updates

Abstract: Transverse momentum spectra of negative and positive pions produced at mid-(pseudo)rapidity in inelastic or non-single-diffractive proton-proton collisions over a center-of-mass energy, $\sqrt{s}$, range from a few GeV to above 10 TeV are analyzed by the blast-wave fit with Boltzmann (Tsallis) distribution. The blast-wave fit results are well fitting to the experimental data measured by several collaborations. In a particular superposition with Hagedorn function, both the excitation functions of kinetic freeze-out temperature (T_0) of emission source and transverse flow velocity (β_T) of produced particles obtained from a given selection in the blast-wave fit with Boltzmann distribution have a hill at $\sqrt{s} \approx 10$ GeV, a drop at dozens of GeV, and then an increase from dozens of GeV to above 10 TeV. However, both the excitation functions of T_0 and β_T obtained in the blast-wave fit with Tsallis distribution do not show such a complex structure, but a very low hill. In another selection for the parameters or in the superposition with the usual step function, T_0 and β_T increase generally quickly from a few GeV to about 10 GeV and then slightly at above 10 GeV, there is no such the complex structure, when also studying nucleus-nucleus collisions.

Keywords: excitation function of kinetic freeze-out temperature; excitation function of transverse flow velocity; proton–proton collisions

PACS: 14.40.Aq; 13.85.Hd; 13.75.Cs

1. Introduction

Chemical and thermal or kinetic freeze-outs are two of important stages of system evolution in high energy collisions. The excitation degrees of interacting system at the two stages are possibly different from each other. To describe different excitation degrees of interacting system at the two stages, one can use chemical and kinetic freeze-out temperatures respectively. Generally, at the stage of chemical freeze-out, the ratios of different types of particles are no longer changed, and the chemical freeze-out temperature can be obtained from the ratios of different particles in the framework of thermal model [1–3]. At the stage of kinetic freeze-out, the transverse momentum spectra of different particles are no longer changed, and the dissociation temperature [4] or kinetic freeze-out temperature can be obtained from the transverse momentum spectra according to the hydrodynamical model [4] and the subsequent blast-wave fit with Boltzmann distribution [5–7] or with Tsallis distribution [8–10].

It should be pointed out that the transverse momentum spectra even though in narrow range contain both the contributions of random thermal motion and transverse flow of particles. The random thermal motion and transverse flow reflect the excitation and expansion degrees of the interacting system (or emission source) respectively. To extract the kinetic freeze-out temperature from transverse

momentum spectra, we have to exclude the contribution of transverse flow, that is, we have to disengage the random thermal motion and transverse flow. There are more than one methods to disengage the two issues [4]. The simplest and easiest method is to use the blast-wave fit with Boltzmann distribution [5–7] and with Tsallis distribution [8–10] to analyze the transverse momentum spectra, though other method such as the alternative method [6,11–17] can obtain similar results [18].

The early blast-wave fit is based on the Boltzmann distribution [5–7]. An alternative blast-wave fit is used due to the Tsallis distribution [8–10]. Both types of blast-wave fit can be used to disengage the random thermal motion and transverse flow. Then, the kinetic freeze-out temperature of interacting system and transverse flow velocity of light flavor particles can be extracted. Most of light flavor particles are produced in soft excitation process and have narrow transverse momentum range up to 2∼3 GeV/c. A few part of light flavor particles are produced in hard scattering process and have higher transverse momenta. Generally, heavy flavor particles are produced via hard scattering process. From the point of view of disengaging or extraction, particles produced in hard scattering process are not needed to consider by us.

The excitation function of kinetic freeze-out temperature, that is, the dependence of kinetic freeze-out temperature on collision energy, is very interesting for us to study the properties of high energy collisions. We think that the particular change of excitation functions of kinetic freeze-out temperature and other parameters are related to the critical-end-point (CEP) of phase transition from hadronic matter to quark-gluon plasma (QGP or quark matter) happened in central nucleus-nucleus (AA or A-A) collisions, where the particular change means the appearances of saturation, minimum, maximum, knee point, asymptotical line, etc. For high multiplicity proton–proton (pp or p-p) collisions, even for minimum-bias pp collisions, the particular change of excitation functions of some parameters are expected to compare with those in AA collisions, where the quark degree of freedom in minimum-bias pp collisions is expected to play initially a main role at the energy of particular change, though QGP is not expected to form in minimum-bias pp collisions due to small system and products. The minimum of excitation function is also related to the soft point of equation of state (EOS) of hadronic matter or QGP, which is also related to the phase transition.

Although there are many studies on the excitation functions of kinetic freeze-out temperature and other parameters, the results seem to be inconsistent. For example, over a center-of-mass energy per nucleon pair, $\sqrt{s_{NN}}$, range from a few GeV to a few TeV, the excitation function of kinetic freeze-out temperature in gold-gold (Au-Au) and lead-lead (Pb-Pb) collisions initially increases and then inconsistently saturates [19,20], increases [21], or decreases [22,23] with the increase of collision energy. On the contrary, the excitation function of the chemical freeze-out temperature shows initially increases and then consistently saturates with collision energy [1–4]. Comparatively, as the basic processes in AA collisions, pp collisions are very important in the study of the mentioned excitation functions. However, the excitation functions in pp collisions are short of studies. We hope to study the particular changes of excitation functions in pp collisions due to they being also related to quark degree of freedom, but not QGP. Indeed, it is worth to study the excitation functions of kinetic freeze-out temperature and other parameters in pp collisions and to judge their tendencies over an energy range from GeV to TeV.

In this paper, by using the blast-wave fit with Boltzmann distribution [5–7] and with Tsallis distribution [8–10], we study the excitation functions of some concerned quantities in inelastic (INEL) or non-single-diffractive (NSD) pp collisions which are closer to peripheral nuclear collisions comparing with central ones. The experimental transverse momentum spectra of negative and positive pions (π^- and π^+) measured mainly at the mid-rapidity by the NA61/SHINE Collaboration [24] at the the Super Proton Synchrotron (SPS) and its beam energy scan (BES) program, the PHENIX [25] and STAR [6] Collaborations at the Relativistic Heavy Ion Collider (RHIC), as well as the ALICE [26] and CMS [27,28] Collaborations at the Large Hadron Collider (LHC) are analyzed, while the data in the forward and backward rapidity regions are not available in most cases.

The remainder of this paper is structured as follows. The formalism and method are shortly described in Section 2. Results and discussion are given in Section 3. In Section 3.1, we summarize our main observations and conclusions.

2. Formalism and Method

There are two main processes of particle productions, namely the soft excitation process and the hard scattering process, in high energy collisions. For the soft excitation process, the method used in the present work is the blast-wave fit [5–10] that has wide applications in particle productions. The blast-wave fit is based on two types of distributions. One is the Boltzmann distribution [5–7] and another one is the Tsallis distribution [8–10]. As an application of the blast-wave fit, we present directly its formalisms in the following. Although the blast-wave fit has abundant connotations, we focus only our attention on the formalism of transverse momentum (p_T) distribution in which the kinetic freeze-out temperature (T_0) and mean transverse flow velocity (β_T) are included.

We are interested in the blast-wave fit with Boltzmann distribution in its original form. According to [5–7], the blast-wave fit with Boltzmann distribution results in the probability density distribution of p_T to be

$$f_1(p_T) = \frac{1}{N}\frac{dN}{dp_T} = C_1 p_T m_T \int_0^R r dr \times$$
$$I_0\left[\frac{p_T \sinh(\rho)}{T_0}\right] K_1\left[\frac{m_T \cosh(\rho)}{T_0}\right], \tag{1}$$

where C_1 is the normalized constant, $m_T = \sqrt{p_T^2 + m_0^2}$ is the transverse mass, m_0 is the rest mass, r is the radial coordinate in the thermal source, R is the maximum r which can be regarded as the transverse size of source in the case of neglecting the expansion, r/R is the relative radial position which has in fact more meanings than r and R themselves, I_0 and K_1 are the modified Bessel functions of the first and second kinds respectively, $\rho = \tanh^{-1}[\beta(r)]$ is the boost angle, $\beta(r) = \beta_S(r/R)^{n_0}$ is a self-similar flow profile, β_S is the flow velocity on the surface, and $n_0 = 2$ is used in the original form [5]. There is the relation between β_T and $\beta(r)$. As a mean of $\beta(r)$, $\beta_T = (2/R^2)\int_0^R r\beta(r)dr = 2\beta_S/(n_0 + 2)$.

We are also interested in the blast-wave fit with Tsallis distribution in its original form. According to [8–10], the blast-wave fit with Tsallis distribution results in the p_T distribution to be

$$f_2(p_T) = \frac{1}{N}\frac{dN}{dp_T} = C_2 p_T m_T \int_{-\pi}^{\pi} d\phi \int_0^R r dr \Big\{1 +$$
$$\frac{q-1}{T_0}\left[m_T \cosh(\rho) - p_T \sinh(\rho)\cos(\phi)\right]\Big\}^{-1/(q-1)}, \tag{2}$$

where C_2 is the normalized constant, q is an entropy index that characterizes the degree of non-equilibrium, ϕ denotes the azimuthal angle, and $n_0 = 1$ is used in the original form [8]. Because of n_0 being an insensitive quantity, the results corresponding to $n_0 = 1$ and 2 for the blast-wave fit with Boltzmann or Tsallis distribution are harmonious [18]. In fact, in some literature [29], n_0 is regarded as a free parameter which changes largely by several times and increases 1 in the number of free parameter, which is not our expectation in the present work. In addition, the index $-1/(q-1)$ used in Equation (2) can be replaced by $-q/(q-1)$ due to q being very close to 1. This substitution results in a small and negligible difference in the Tsallis distribution [30,31].

For a not too wide p_T spectrum, the above two equations can be used to describe the p_T spectrum and to extract T_0 and β_T. For a wide p_T spectrum, we have to consider the contribution of hard scattering process. According to the quantum chromodynamics (QCD) calculus [32–34], the contribution of hard scattering process is parameterized to be an inverse power-law

$$f_H(p_T) = \frac{1}{N}\frac{dN}{dp_T} = A p_T \left(1 + \frac{p_T}{p_0}\right)^{-n} \tag{3}$$

which is the Hagedorn function [35,36], where p_0 and n are free parameters, and A is the normalization constant related to the free parameters. In literature [37–43], there are respectively modified Hagedorn functions

$$f_H(p_T) = \frac{1}{N}\frac{dN}{dp_T} = A\frac{p_T^2}{m_T}\left(1 + \frac{p_T}{p_0}\right)^{-n},\tag{4}$$

$$f_H(p_T) = \frac{1}{N}\frac{dN}{dp_T} = Ap_T\left(1 + \frac{p_T^2}{p_0^2}\right)^{-n},\tag{5}$$

and

$$f_H(p_T) = \frac{1}{N}\frac{dN}{dp_T} = A\left(1 + \frac{p_T^2}{p_0^2}\right)^{-n},\tag{6}$$

where the three normalization constants A, free parameters p_0, and free parameters n are severally different, though the same symbols are used to avoid trivial expression.

The experimental p_T spectrum distributed in a wide range can be described by a superposition of the contributions of the soft excitation and hard scattering processes. If one of Equations (1) and (2) describes the contribution of the soft excitation process, one of Equations (3)–(6) describes the contribution of the hard scattering process. To describe the spectrum in a wide p_T range, we can superpose a two-component superposition like this

$$f_0(p_T) = kf_S(p_T) + (1 - k)f_H(p_T),\tag{7}$$

where k $(1 - k)$ denotes the contribution fraction of the soft excitation (hard scattering) process, and $f_S(p_T)$ denotes one of Equations (1) and (2). As for the four $f_H(p_T)$, we are inclined to the first one due to its more applications. Naturally, we have the normalization condition $\int_0^{p_{T\max}} f_0(p_T)dp_T = 1$, where $p_{T\max}$ denotes the maximum p_T. In Equation (7), the soft component contributes in low p_T region and the hard component contributes in whole p_T range. The two contributions overlap each other in low p_T region.

According to Hagedorn's model [35], we may also use the usual step function to superpose the two functions. That is

$$f_0(p_T) = A_1\theta(p_1 - p_T)f_S(p_T) + A_2\theta(p_T - p_1)f_H(p_T),\tag{8}$$

where A_1 and A_2 are constants which result in the two components to be equal to each other at $p_T = p_1 \approx 2 \sim 3$ GeV/c. The contribution fraction of the soft excitation (hard excitation) process in Equation (8) is $k = \int_0^{p_1} A_1 f_S(p_T)dp_T$ $[1 - k = \int_{p_1}^{p_{T\max}} A_2 f_H(p_T)dp_T]$ due to $\int_0^{p_{T\max}} f_0(p_T)dp_T = 1$. In Equation (8), the soft component contributes in low p_T region and the hard component contributes in high p_T region. The two contributions link with each other at $p_T = p_1$.

In some cases, the contribution of resonance production for pions in very-low p_T range has to be considered. We can use a very-soft component for the p_T range from 0 to 0.2~0.3 GeV/c which covers the contribution of resonance production. Let k_{VS} and k_S denote the contribution fractions of the very-soft and soft processes respectively. Equation (7) is revised to

$$\begin{aligned}f_0(p_T) =&k_{VS}f_{VS}(p_T) + k_S f_S(p_T)\\&+ (1 - k_{VS} - k_S)f_H(p_T),\end{aligned}\tag{9}$$

where $f_{VS}(p_T)$ denotes one of Equations (1) and (2) as $f_S(p_T)$, but having smaller parameter values comparing with $f_S(p_T)$. Anyhow, both the very-soft and soft processes are belong to the soft process. Correspondingly, Equation (8) is revised to

$$\begin{aligned}
f_0(p_T) =&\, A_1\theta(p_1 - p_T)f_{VS}(p_T) \\
&+ A_2\theta(p_T - p_1)\theta(p_2 - p_T)f_S(p_T) \\
&+ A_3\theta(p_T - p_2)f_H(p_T),
\end{aligned} \tag{10}$$

where A_1, A_2, and A_3 are constants which result in the two contiguous components to be equal to each other at $p_T = p_1$ and $p_T = p_2$.

The above two types of superpositions [Equations (7) and (8)] treat the soft and hard components by different ways in the whole p_T range. Equation (7) means that the soft component contributes in a range from 0 up to 2∼3 GeV/c or a little more. The hard component contributes in the whole p_T range, though the main contributor in the low p_T region is the soft component and the sole contributor in the high p_T region is the hard component. Equation (8) shows that the soft component contributes in a range from 0 up to p_1, and the hard component contributes in a range from p_1 up to the maximum. The boundary of the contributions of soft and hard components is p_1. There is no mixed region for the two components in Equation (8).

In the case of including only the soft component, Equations (7) and (8) are the same. In the case of including both the soft and hard components, their common parameters such as T_0, β_T, p_0, and n should be severally to have small differences from each other. To avoid large differences, we should select the experimental data in a narrow p_T range. In addition, the very-soft component in Equations (9) and (10) does not need to consider in some cases due to the fact that the spectrum in very-low p_T range are possibly not available in experiment. Then, Equations (9) and (10) are degenerated to Equations (7) and (8) respectively in some cases.

In the fit process, firstly, we use Equation (7) to extract the related parameters, where $f_S(p_T)$ and $f_H(p_T)$ are exactly Equations (1) or (2) and (3) respectively. Regardless of Equation (1) or (2) is regarded as $f_S(p_T)$, the situation is similar due to Equations (1) and (2) being harmonious in trends of parameters [18], though one more parameter (the entropy index q) is needed in Equation (2). Secondly, we use Equation (8) to extract the related parameters as comparisons with those from Equations (7). In the case of Equations (7) and (8) being not suitable, Equations (9) and (10) can be used due to the very-low component from resonance decays being included in the first items of the two fits. Meanwhile, the contribution of resonance decays in the low component is naturally included in the second items of Equations (9) and (10) or in the first items of Equations (7) and (8). Thus, the contribution of resonance decays which is available in the very-low or low component in experiment is naturally considered by us.

It should be pointed out that although Equations (9) and (10) are not used in the final fits in the present work, we hope to keep them here due to the fact that we need them to give further explanations. From theses explanations, one can see the relations between Equations (9)/(10) and (7)/(8), as well as possible applications of Equations (9) and (10).

3. Results and Discussion

3.1. Comparison with Data by Equation (7)

Figure 1 shows the transverse momentum spectra of π^- and π^+ produced at mid-(pseudo)rapidity in pp collisions at high center-of-mass energies, where different mid-(pseudo)rapidity (y or η) intervals and energies ($\sqrt{s}$) are marked in the panels. Different forms of the spectra are used due to different Collaborations, where N, E, p, σ, and N_{EV} denote the particle number, energy, momentum, cross-section, and event number, respectively. The closed and open symbols presented in panels (a)–(e) represent the data of π^- and π^+ measured by the NA61/SHINE [24], PHENIX [25], STAR [6], ALICE [26], and CMS [27,28] Collaborations, respectively, where in panel (a) only the spectra of π^- are available, and panel (c) is for NSD events and other panels are for INEL events. Although the pp collisions are divided on the multiplicity classes in experiments on the LHC, we have used the minimum-bias INEL events [26–28] which can be regarded

as the combination of the events in different multiplicity classes with different yields. We regret not using the ATLAS Collaboration results [44–48] given no data on the p_T spectra of π^- and π^+. These data show wider p_T spectra of charged particles to be used in our foreseen studies. In some cases, different amounts marked in the panels are used to scale the data for clarity. We have fitted the data by two sets of parameter values in Equation (7) so that we can see the fluctuations of parameter values. The blue solid (dotted) curves are our results for π^- (π^+) spectra fitted by Equation (7) through Equations (1) and (3), and the blue dashed (dot-dashed) curves are our results for π^- (π^+) spectra fitted by Equation (7) through Equations (2) and (3), by the first set of parameter values, in which k is taken to close to 0.5 as much as possible. The black curves are our results fitted by the second set of parameter values for comparison, in which k is taken to close to 1 as much as possible. The values of free parameters (T_0, β_T, q if available, k, p_0, and n), normalization constant (N_0), χ^2, and number of degrees of freedom (ndof) corresponding to the curves in Figure 1 are listed in Tables 1 and 2, where the errors of fit parameters are obtained by the statistical simulation method [49], no matter what χ^2/ndof is. The parameter values presented in terms of value$_1$/value$_2$ denote respectively the first and second sets of parameter values in Equation (7) through Equations (1)–(3) in which $k \neq 1$. One can see that Equation (7) with two sets of parameter values describes the p_T spectra at mid-(pseudo)rapidity in pp collisions over an energy range from a few GeV to above 10 TeV. The blast-wave fit with Boltzmann distribution and with Tsallis distribution presents similar results. The free parameters show some laws in the considered energy range. For a given parameter, its fluctuation at given energy is obvious in some cases. Because of the data being not available in very-low p_T range, Equation (9) is not used in the fit.

It should be noted that, from the fit process we know that, the Tsallis expression, Equation (2), having a polynomial behavior at large p_T could be a better description for the spectra at large values of p_T, where the Boltzmann expression, Equation (1) does not work possibly at large p_T if we use the same parameters T_0 and β_T. In some cases, for the spectra in a wide p_T range, a single Tsallis expression is suitable, and two- or three-component Boltzmann expression is needed. Our previous work [50] studied both the Tsallis and Boltzmann distributions without flow effect and also confirms this issue. Indeed, the Tsallis description is better than the Boltzmann one, though the former has one more parameter q. In fact, the introduction of the entropy index q in the Tsallis description has the meaning of reality. As discussed in Section 2, q characterizes the degree of non-equilibrium. In addition, when $q \to 1$, the Tsallis description degenerates to the Boltzmann one.
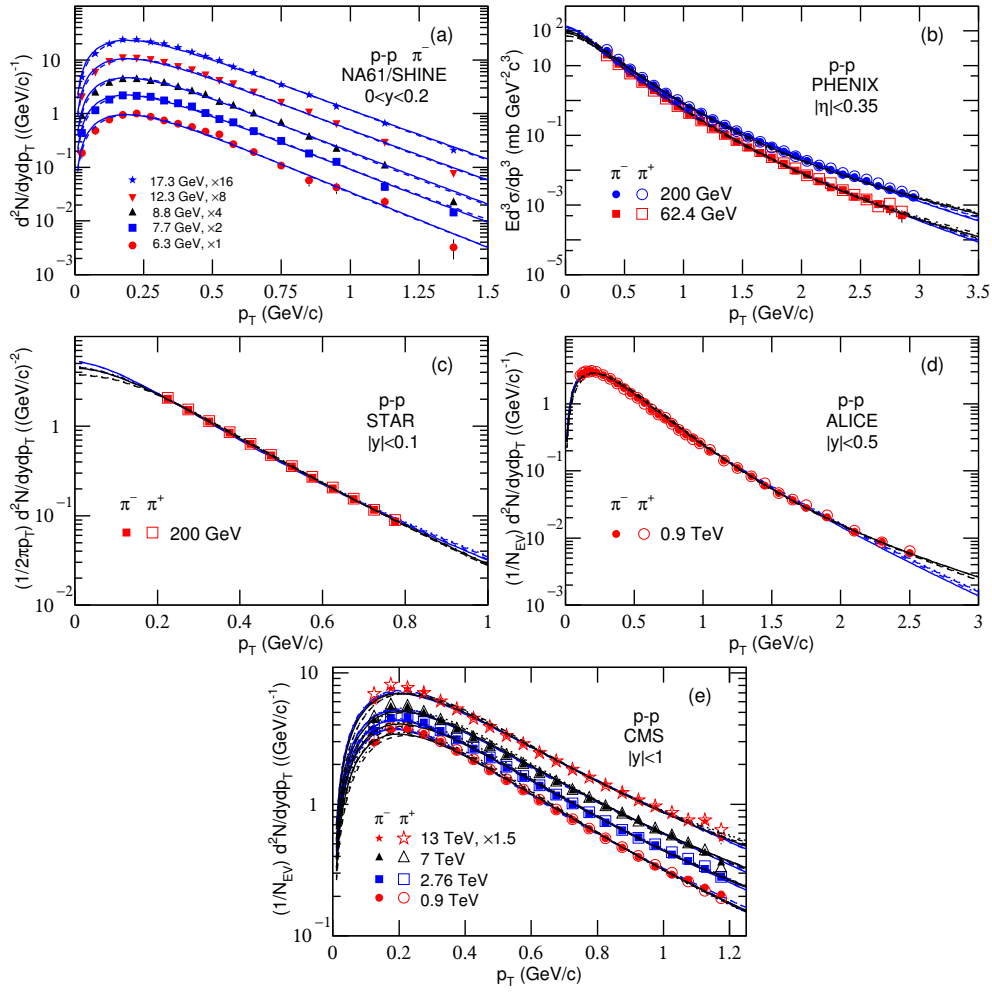
Figure 1. Transverse momentum spectra of π^- and π^+ produced at mid-(pseudo)rapidity in *pp* collisions at high energies, where the mid-(pseudo)rapidity intervals and energies are marked in the panels. The symbols presented in panels (**a**–**e**) represent the data of NA61/SHINE [24], PHENIX [25], STAR [6], ALICE [26], and CMS [27,28] Collaborations, respectively, where in panel (**a**) only the spectra of π^- are available, and panel (**c**) is for NSD events and other panels are for INEL events. Although the *pp* collisions are divided on the multiplicity classes in experiments on the LHC, we have used the minimum-bias INEL events [26–28]. In some cases, different amounts marked in the panels are used to scale the data for clarity. The blue solid (dotted) curves are our results for π^- (π^+) spectra fitted by Equation (7) through Equations (1) and (3), and the blue dashed (dot-dashed) curves are our results for π^- (π^+) spectra fitted by Equation (7) through Equations (2) and (3), by the first set of parameter values. The results by the second set of parameters (if available) are presented by the black curves.

Table 1. Values of free parameters (T_0, β_T, k, p_0, and n), normalization constant (N_0), χ^2, and ndof corresponding to the solid (dotted) curves for π^- (π^+) spectra in Figure 1 in which different data are measured in different mid-(pseudo)rapidity intervals at different energies by different Collaborations. The values presented in terms of value$_1$/value$_2$ denote respectively the first and second sets of parameter values in Equation (7) through Equations (1) and (3) in which $k \neq 1$.

Collab.	$\sqrt{s}$ (GeV)	Part.	T_0 (MeV)	β_T (c)	k	p_0 (GeV/c)	n	N_0	χ^2	ndof
NA61/	6.3	π^-	108 ± 5	0.30 ± 0.02	1	–	–	0.08 ± 0.01	21	15
SHINE	7.7	π^-	109 ± 5	0.31 ± 0.02	1	–	–	0.10 ± 0.01	34	15
INEL	8.8	π^-	110 ± 5	0.31 ± 0.02	1	–	–	0.10 ± 0.01	73	15
	12.3	π^-	111 ± 6	0.32 ± 0.02	1	–	–	0.12 ± 0.01	59	15
	17.3	π^-	112 ± 6	0.33 ± 0.02	1	–	–	0.13 ± 0.01	26	15
PHENIX	62.4	π^-	$96 \pm 5/114 \pm 6$	$0.27 \pm 0.01/0.34 \pm 0.02$	$0.66 \pm 0.01/0.98 \pm 0.01$	$3.60 \pm 0.18/6.06 \pm 0.30$	$19.23 \pm 0.96/18.63 \pm 0.93$	$21.55 \pm 1.08/18.96 \pm 0.95$	7/28	20
INEL		π^+	$96 \pm 5/114 \pm 6$	$0.27 \pm 0.01/0.34 \pm 0.02$	$0.66 \pm 0.01/0.98 \pm 0.01$	$3.63 \pm 0.18/6.07 \pm 0.30$	$19.03 \pm 0.95/18.63 \pm 0.93$	$20.81 \pm 1.04/18.57 \pm 0.93$	11/11	20
	200	π^-	$100 \pm 5/116 \pm 5$	$0.30 \pm 0.02/0.36 \pm 0.02$	$0.62 \pm 0.01/0.96 \pm 0.02$	$4.19 \pm 0.21/6.45 \pm 0.32$	$19.01 \pm 0.95/18.01 \pm 0.90$	$23.98 \pm 1.20/22.77 \pm 1.14$	26/21	21
		π^+	$100 \pm 5/115 \pm 5$	$0.30 \pm 0.02/0.35 \pm 0.02$	$0.62 \pm 0.01/0.96 \pm 0.02$	$4.21 \pm 0.21/6.46 \pm 0.32$	$19.01 \pm 0.95/18.00 \pm 0.90$	$24.41 \pm 1.22/24.41 \pm 1.22$	54/26	21
STAR	200	π^-	$98 \pm 6/112 \pm 5$	$0.29 \pm 0.02/0.34 \pm 0.02$	$0.61 \pm 0.03/0.98 \pm 0.02$	$4.01 \pm 0.20/6.00 \pm 0.30$	$19.21 \pm 0.96/18.61 \pm 0.93$	$0.27 \pm 0.01/0.92 \pm 0.05$	76/3	6
NSD		π^+	$99 \pm 6/112 \pm 5$	$0.29 \pm 0.02/0.34 \pm 0.02$	$0.60 \pm 0.03/0.98 \pm 0.02$	$4.01 \pm 0.20/6.00 \pm 0.30$	$19.21 \pm 0.96/18.61 \pm 0.93$	$0.27 \pm 0.01/0.27 \pm 0.01$	96/4	6
ALICE	900	π^-	$101 \pm 5/116 \pm 6$	$0.31 \pm 0.02/0.36 \pm 0.02$	$0.63 \pm 0.02/0.94 \pm 0.02$	$4.39 \pm 0.22/6.81 \pm 0.34$	$18.89 \pm 0.94/17.35 \pm 0.87$	$1.47 \pm 0.07/1.47 \pm 0.07$	38/126	27
INEL		π^+	$101 \pm 5/116 \pm 6$	$0.31 \pm 0.02/0.35 \pm 0.02$	$0.63 \pm 0.02/0.95 \pm 0.02$	$4.42 \pm 0.22/6.96 \pm 0.35$	$18.81 \pm 0.94/17.35 \pm 0.87$	$1.47 \pm 0.07/1.47 \pm 0.07$	49/137	27
CMS	900	π^-	$101 \pm 5/115 \pm 6$	$0.31 \pm 0.02/0.35 \pm 0.02$	$0.63 \pm 0.03/0.91 \pm 0.02$	$4.43 \pm 0.22/7.08 \pm 0.35$	$18.71 \pm 0.93/17.13 \pm 0.87$	$3.65 \pm 0.18/3.49 \pm 0.17$	24/62	16
INEL		π^+	$101 \pm 5/115 \pm 5$	$0.31 \pm 0.02/0.35 \pm 0.02$	$0.63 \pm 0.03/0.92 \pm 0.02$	$4.43 \pm 0.22/7.04 \pm 0.35$	$18.71 \pm 0.93/17.16 \pm 0.86$	$3.70 \pm 0.19/3.55 \pm 0.18$	16/59	16
	2760	π^-	$103 \pm 6/116 \pm 4$	$0.33 \pm 0.02/0.36 \pm 0.02$	$0.63 \pm 0.03/0.90 \pm 0.02$	$4.68 \pm 0.23/7.80 \pm 0.39$	$18.41 \pm 0.92/16.45 \pm 0.82$	$4.47 \pm 0.22/4.31 \pm 0.22$	34/70	16
		π^+	$102 \pm 6/116 \pm 5$	$0.33 \pm 0.02/0.36 \pm 0.02$	$0.63 \pm 0.04/0.91 \pm 0.02$	$4.69 \pm 0.23/7.90 \pm 0.39$	$18.39 \pm 0.92/16.35 \pm 0.82$	$4.55 \pm 0.23/4.43 \pm 0.22$	35/74	16
	7000	π^-	$104 \pm 5/117 \pm 6$	$0.34 \pm 0.02/0.37 \pm 0.02$	$0.62 \pm 0.03/0.89 \pm 0.02$	$4.79 \pm 0.24/8.00 \pm 0.40$	$18.21 \pm 0.91/16.13 \pm 0.81$	$5.50 \pm 0.27/5.49 \pm 0.27$	48/67	16
		π^+	$103 \pm 5/116 \pm 4$	$0.34 \pm 0.02/0.36 \pm 0.02$	$0.61 \pm 0.04/0.89 \pm 0.02$	$4.80 \pm 0.24/8.20 \pm 0.41$	$18.21 \pm 0.91/16.00 \pm 0.80$	$5.54 \pm 0.28/5.52 \pm 0.28$	55/70	16
	13000	π^-	$105 \pm 5/117 \pm 5$	$0.35 \pm 0.02/0.37 \pm 0.02$	$0.61 \pm 0.03/0.89 \pm 0.02$	$4.90 \pm 0.24/8.30 \pm 0.41$	$18.11 \pm 0.90/15.99 \pm 0.80$	$5.07 \pm 0.25/5.07 \pm 0.25$	30/28	16
		π^+	$104 \pm 5/117 \pm 5$	$0.34 \pm 0.02/0.36 \pm 0.02$	$0.64 \pm 0.04/0.88 \pm 0.02$	$5.00 \pm 0.25/8.99 \pm 0.43$	$18.00 \pm 0.90/15.59 \pm 0.78$	$5.12 \pm 0.26/5.15 \pm 0.26$	36/42	16

Table 2. Values of free parameters (T_0, β_T, q k, p_0, and n), normalization constant (N_0), χ^2, and ndof corresponding to the dashed (dot-dashed) curves for π^- (π^+) spectra in Figure 1 in which different data are measured in different mid-(pseudo)rapidity intervals at different energies by different Collaborations. The values presented in terms of value$_1$/value$_2$ denote respectively the first and second sets of parameter values in Equation (7) through Equations (2) and (3) in which $k \neq 1$.

Collab.	$\sqrt{s}$ (GeV)	Part.	T_0 (MeV)	β_T (c)	q	p_0 (GeV/c)	n	N_0	χ^2		ndof
NA61/ SHINE INEL	6.3	π^-	81 ± 4	0.19 ± 0.01	1.05 ± 0.002	1	–	–	0.08 ± 0.01	12	14
	7.7	π^-	81 ± 4	0.20 ± 0.01	1.06 ± 0.002	1	–	–	0.10 ± 0.01	13	14
	8.8	π^-	83 ± 4	0.20 ± 0.01	1.05 ± 0.002	1	–	–	0.10 ± 0.01	24	14
	12.3	π^-	84 ± 4	0.21 ± 0.01	1.06 ± 0.002	1	–	–	0.12 ± 0.01	14	14
	17.3	π^-	85 ± 4	0.21 ± 0.01	1.06 ± 0.002	1	–	–	0.13 ± 0.01	5	14
PHENIX INEL	62.4	π^-	$78 \pm 4/86 \pm 4$	$0.18 \pm 0.01/0.21 \pm 0.01$	$1.04 \pm 0.01/1.06 \pm 0.01$	$0.63 \pm 0.03/0.98 \pm 0.05$	$3.02 \pm 0.15/5.36 \pm 0.27$	$16.99 \pm 0.85/18.73 \pm 0.94$	$19.53 \pm 0.98/18.26 \pm 0.91$	16/18	19
		π^+	$79 \pm 5/85 \pm 4$	$0.18 \pm 0.01/0.21 \pm 0.01$	$1.04 \pm 0.01/1.06 \pm 0.01$	$0.63 \pm 0.02/0.97 \pm 0.05$	$3.10 \pm 0.15/5.36 \pm 0.27$	$16.99 \pm 0.85/18.73 \pm 0.94$	$18.42 \pm 0.92/18.26 \pm 0.91$	30/23	19
	200	π^-	$80 \pm 5/86 \pm 4$	$0.19 \pm 0.01/0.23 \pm 0.01$	$1.02 \pm 0.01/1.06 \pm 0.01$	$0.59 \pm 0.02/0.95 \pm 0.05$	$3.53 \pm 0.17/5.99 \pm 0.30$	$16.68 \pm 0.84/18.23 \pm 0.91$	$24.48 \pm 1.22/23.86 \pm 1.19$	39/24	20
		π^+	$80 \pm 5/86 \pm 4$	$0.19 \pm 0.01/0.23 \pm 0.01$	$1.02 \pm 0.01/1.06 \pm 0.01$	$0.59 \pm 0.03/0.95 \pm 0.05$	$3.53 \pm 0.17/6.09 \pm 0.30$	$16.68 \pm 0.84/18.23 \pm 0.91$	$25.07 \pm 1.25/24.49 \pm 1.22$	45/68	20
STAR NSD	200	π^-	$79 \pm 5/85 \pm 4$	$0.19 \pm 0.01/0.23 \pm 0.01$	$1.04 \pm 0.01/1.05 \pm 0.01$	$0.62 \pm 0.03/0.95 \pm 0.05$	$3.70 \pm 0.18/5.89 \pm 0.29$	$16.68 \pm 0.82/18.43 \pm 0.92$	$0.26 \pm 0.01/0.26 \pm 0.01$	22/39	5
		π^+	$79 \pm 4/85 \pm 4$	$0.19 \pm 0.01/0.23 \pm 0.01$	$1.04 \pm 0.01/1.05 \pm 0.01$	$0.62 \pm 0.02/0.95 \pm 0.05$	$3.70 \pm 0.18/5.89 \pm 0.29$	$16.68 \pm 0.82/18.43 \pm 0.92$	$0.27 \pm 0.01/0.26 \pm 0.01$	15/28	5
ALICE INEL	900	π^-	$81 \pm 5/86 \pm 4$	$0.20 \pm 0.01/0.25 \pm 0.01$	$1.03 \pm 0.01/1.06 \pm 0.01$	$0.53 \pm 0.02/0.93 \pm 0.05$	$3.63 \pm 0.19/6.39 \pm 0.32$	$16.68 \pm 0.81/18.03 \pm 0.90$	$1.47 \pm 0.07/1.47 \pm 0.07$	34/419	26
		π^+	$80 \pm 3/86 \pm 4$	$0.20 \pm 0.01/0.25 \pm 0.01$	$1.03 \pm 0.01/1.06 \pm 0.01$	$0.53 \pm 0.03/0.93 \pm 0.05$	$3.64 \pm 0.19/6.39 \pm 0.32$	$16.68 \pm 0.81/18.03 \pm 0.90$	$1.50 \pm 0.08/1.50 \pm 0.08$	51/558	26
CMS INEL	900	π^-	$81 \pm 3/87 \pm 4$	$0.19 \pm 0.01/0.25 \pm 0.01$	$1.02 \pm 0.01/1.05 \pm 0.01$	$0.51 \pm 0.03/0.89 \pm 0.05$	$3.74 \pm 0.19/6.79 \pm 0.34$	$16.68 \pm 0.80/17.83 \pm 0.89$	$3.67 \pm 0.18/3.45 \pm 0.17$	8/124	15
		π^+	$80 \pm 4/87 \pm 4$	$0.19 \pm 0.01/0.25 \pm 0.01$	$1.02 \pm 0.01/1.05 \pm 0.01$	$0.51 \pm 0.02/0.89 \pm 0.05$	$3.72 \pm 0.19/6.79 \pm 0.34$	$16.68 \pm 0.80/17.83 \pm 0.89$	$3.74 \pm 0.19/3.59 \pm 0.18$	6/121	15
	2760	π^-	$81 \pm 5/88 \pm 4$	$0.21 \pm 0.01/0.26 \pm 0.01$	$1.02 \pm 0.01/1.05 \pm 0.01$	$0.49 \pm 0.02/0.86 \pm 0.05$	$3.96 \pm 0.20/7.49 \pm 0.37$	$16.56 \pm 0.80/17.47 \pm 0.87$	$4.46 \pm 0.22/4.24 \pm 0.21$	15/114	15
		π^+	$81 \pm 5/88 \pm 4$	$0.21 \pm 0.01/0.26 \pm 0.01$	$1.02 \pm 0.01/1.05 \pm 0.01$	$0.49 \pm 0.03/0.86 \pm 0.05$	$3.92 \pm 0.20/7.49 \pm 0.37$	$16.55 \pm 0.80/17.47 \pm 0.87$	$4.56 \pm 0.23/4.44 \pm 0.22$	15/115	15
	7000	π^-	$83 \pm 4/89 \pm 4$	$0.21 \pm 0.01/0.27 \pm 0.01$	$1.02 \pm 0.01/1.05 \pm 0.01$	$0.47 \pm 0.02/0.84 \pm 0.05$	$3.98 \pm 0.19/7.69 \pm 0.38$	$16.30 \pm 0.81/17.37 \pm 0.87$	$5.55 \pm 0.28/5.41 \pm 0.27$	23/129	15
		π^+	$82 \pm 4/87 \pm 4$	$0.21 \pm 0.01/0.26 \pm 0.01$	$1.02 \pm 0.01/1.05 \pm 0.01$	$0.47 \pm 0.03/0.84 \pm 0.05$	$3.99 \pm 0.19/7.59 \pm 0.38$	$16.37 \pm 0.81/17.37 \pm 0.87$	$5.60 \pm 0.28/5.60 \pm 0.28$	31/171	15
	13000	π^-	$83 \pm 5/88 \pm 4$	$0.22 \pm 0.01/0.27 \pm 0.01$	$1.02 \pm 0.01/1.05 \pm 0.01$	$0.46 \pm 0.02/0.82 \pm 0.05$	$4.05 \pm 0.20/7.89 \pm 0.39$	$16.31 \pm 0.82/17.27 \pm 0.86$	$5.20 \pm 0.26/5.10 \pm 0.26$	13/50	15
		π^+	$84 \pm 5/86 \pm 4$	$0.23 \pm 0.01/0.27 \pm 0.01$	$1.02 \pm 0.01/1.05 \pm 0.01$	$0.47 \pm 0.03/0.80 \pm 0.05$	$4.09 \pm 0.20/7.99 \pm 0.40$	$16.28 \pm 0.82/17.07 \pm 0.85$	$5.20 \pm 0.26/5.10 \pm 0.26$	27/74	15

To see clearly the excitation functions of free parameters, Figure 2a–e show the dependences of T_0, β_T, p_0, n, and k on $\sqrt{s}$, respectively. The blue and black closed and open symbols represent the parameter values corresponding to π^- and π^+ respectively, which are listed in Tables 1 and 2. The blue circles (black squares) represent the first set of parameter values obtained from Equation (7) through Equations (1)–(3). The blue asterisks (black triangles) represent the second set of parameter values obtained from Equation (7) through Equations (1)–(3). One can see that the difference between the results of π^- and π^+ is not obvious. In the excitation functions of the first set of T_0 and β_T obtained from the blast-wave fit with Boltzmann distribution, there are a hill at $\sqrt{s} \approx 10$ GeV, a drop at dozens of GeV, and then an increase from dozens of GeV to above 10 TeV. In the excitation functions of the first set of T_0 and β_T obtained from the blast-wave fit with Tsallis distribution, there is no the complex structure, but a very low hill. In the excitation functions of the second set of T_0 and β_T, there is a slight increase from about 10 GeV to above 10 TeV. In Equation (7) contained the blast-wave fit with both distributions, in the excitation functions of p_0 and n, there are a slight decrease and increase respectively in the case of the hard component being available. The excitation function of k shows that the contribution $(1 - k)$ of hard component slightly increases from dozens of GeV to above 10 TeV, and it has no contribution at around 10 GeV. At given energies, the fluctuations in a given parameter result in different excitation functions due to different selections. As a comparison, the red asterisks (green triangles) in Figure 2 represent the results from AA collisions which are discussed in detail in the Appendix A. One can see that the results from AA collisions approach to those from pp collisions with the second set of parameters, though only the soft component is used in most cases.

Indeed, $\sqrt{s_{NN}} \approx 10$ GeV is a special energy for AA collisions as indicated by Cleymans [51]. The present work shows that $\sqrt{s} \approx 10$ GeV is also a special energy for pp collisions. In particular, there is a hill in the excitation functions of T_0 and β_T in pp collisions due to a given selection of the parameters. At this energy (11 GeV more specifically [51]), the final state has the highest net baryon density, a transition from a baryon-dominated to a meson-dominated final state takes place, and the ratios of strange particles to mesons show clear and pronounced maximums [51]. These properties result in this special energy.

At 11 GeV, the chemical freeze-out temperature in AA collisions is about 151 MeV [51], and the present work shows that the kinetic freeze-out temperature in pp collisions is about 105 MeV, extracted from the blast-wave fit with Boltzmann distribution. If we do not consider the difference between AA and pp collisions, though cold nuclear effect exists in AA collisions, the chemical freeze-out happens obviously earlier than the kinetic one. According to an ideal fluid consideration, the time evolution of temperature follows $T_f = T_i(\tau_i/\tau_f)^{1/3}$, where T_i ($= 300$ MeV) and τ_i ($= 1$ fm) are the initial temperature and proper time respectively [52,53], and T_f and τ_f denote the final temperature and time respectively, the chemical and kinetic freeze-outs happen at 7.8 and 23.3 fm respectively. It should be noted that in the calculation of τ_f, the Lorentz factor is not considered. If we consider the mean Lorentz factor ($\overline{\gamma} \approx 5$–6) of charged pions in the rest frame of emission source [15–18], the value of freeze-out time will be smaller.
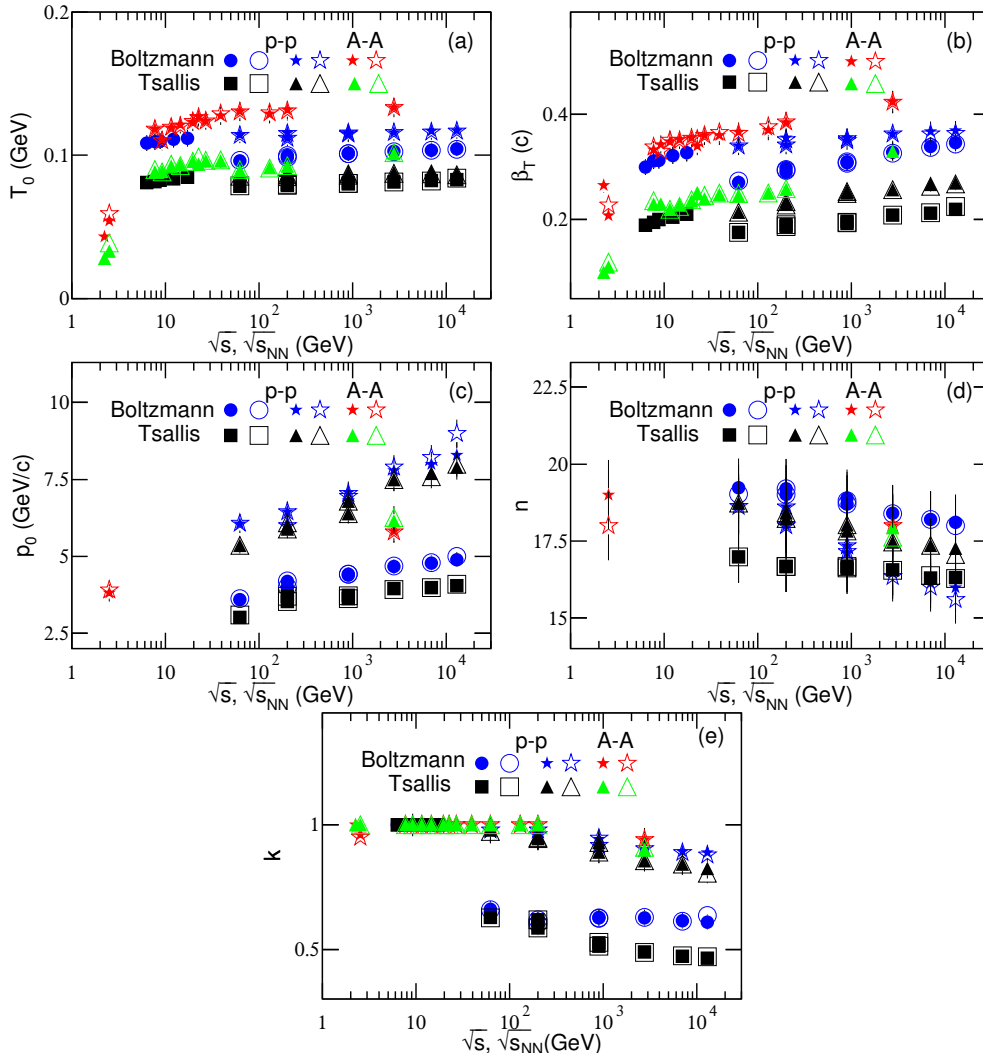
Figure 2. Excitation functions of (**a**) T_0, (**b**) β_T, (**c**) p_0, (**d**) n, and (**e**) k. The closed (open) symbols represent the parameter values corresponding to π^- (π^+) spectra, which are listed in Tables 1 and 2. The blue circles (black squares) represent the first set of parameter values obtained from Equation (7) through Equations (1)–(3). The blue asterisks (black triangles) represent the second set of parameter values obtained from Equation (7) through Equations (1)–(3). The red asterisks (green triangles) represent the parameter values from *AA* collisions for comparisons, which are listed in Tables A1 and A2 in the Appendix A.

Strictly, T_0 (β_T) obtained from the pion spectra in the present work is less than that averaged by weighting the yields of pions, kaons, protons, and other light particles. Fortunately, the fraction of the pion yield in high energy collisions are major ($\approx 85\%$). The parameters and their tendencies obtained from the pion spectra are similar to those obtained from the spectra of all light particles. To study the excitation functions of T_0 and β_T, it does not matter if we use the spectra of pions instead of all light particles.

It should be noted that the main parameters T_0 and β_T are correlated in some way. Although the excitation functions of T_0 (β_T) which are acceptable in the fit process are not sole, their tendencies are harmonious in most cases, in particular in the energy range from the RHIC to LHC. Combining with our previous work [18], we could say that there is a slight ($\approx 10\%$) increase in the excitation function of T_0 and an obvious ($\approx 35\%$) increase in the excitation function of β_T from the RHIC to LHC. At least, the excitation functions of T_0 and β_T do not decrease from the RHIC to LHC.

However, the excitation function of T_0 from low to high energies is not always incremental or invariant, though the excitation function of β_T has the trend of increase in general. For example, In [4], T_0 slowly decreases as $\sqrt{s}$ increases from 23 GeV to 1.8 TeV, and β_T slowly increases with $\sqrt{s}$. In [19,20], T_0 has no obvious change and β_T has a slight ($\approx 10\%$) increase from the RHIC to LHC. In [21], T_0 has a slight ($\approx 9\%$) increase and β_T has a large ($\approx 65\%$) increase from the RHIC to LHC. In [22,23], T_0 has a slight ($\approx 5\%$) decrease from the RHIC to LHC and β_T increases by $\approx 20\%$ from 39 to 200 GeV. It is convinced that β_T increases from the RHIC to LHC, though the situation of T_0 is doubtful.

Although some works [54–57] reported a decrease of T_0 and an increase of β_T from the RHIC to LHC, our re-scans on their plots show a different situation of T_0. For example, in [54], our re-scans show that T_0 has no obvious change and β_T has a slight ($\approx 9\%$) increase from the top RHIC to LHC, though there is an obvious hill or there is an increase by $\approx 30\%$ in T_0 in 5–40 GeV comparting with that at the RHIC. Authors in [55] shows similar results to [54] with the almost invariant T_0 from the top RHIC to LHC, an increase by $\approx 28\%$ in T_0 in 7–40 GeV comparing with that at the top RHIC, and an increase by $\approx 8\%$ in β_T comparing with that at the top RHIC. Authors in [56,57] shows similar result to [54,55] on T_0, though the excitation function of β_T is not available.

In some cases, the correlation between T_0 and β_T are not negative, though some works [54,55] show negative correlation over a wide energy range. For a give p_T spectrum, it seems that a larger T_0 corresponds to a smaller β_T, which shows a negative correlation. However, this negative correlation is not sole case. In fact, a couple of suitable T_0 and β_T can fit a given p_T spectrum. A series of p_T spectra at different energies possibly show a positive correlation between T_0 and β_T, or independent of T_0 on β_T, in a narrow energy range. Very recently, authors in [58] shows approximately independent of T_0 on β_T in pp collisions at $\sqrt{s} = 7$ TeV, and negative correlations in p-Pb collisions at $\sqrt{s_{NN}} = 5.02$ TeV and in Pb-Pb collisions at $\sqrt{s_{NN}} = 2.76$ TeV, for different average charged-particle multiplicity densities, i.e., for different centrality classes. These results are partly in agreement with our results. It seems that the correlation between T_0 and β_T is an open question at present, though some researchers think that there is a negative correlation between T_0 and β_T. In our opinion, the type of correlation between T_0 and β_T depends on three factors, that is the choices of fitted region in low and medium p_T range, fixed or changeable n_0, sensitivity of β_T on centrality. Indeed, more studies are needed in the near future.

To study further the behaviors of parameters, Figure 3 shows the excitation functions of (a)(b) mean p_T ($\langle p_T \rangle$) and (c)(d) ratio of root-mean-square p_T ($\sqrt{\langle p_T^2 \rangle}$) to $\sqrt{2}$, where the left panel [(a)(c)] corresponds to the results of the first component [Equation (1) or (2)] and the right panel [(b)(d)] corresponds to the results of the two components [Equation (7)]. The open symbols (open symbols with asterisks) represent the values corresponding to π^- (π^+) spectra. The blue circles (black squares) represent the values obtained indirectly from Equations (1) and (2) for the left panel or Equation (7) through Equations (1)–(3) for the right panel, by the first set of parameter values. The results by the second set of parameter values are presented by the blue asterisks (black triangles). These values are indirectly obtained from the equations according to the parameters listed in Tables 1 and 2 over a p_T range from 0 to 5 GeV/c which is beyond the available range of the data. If the initial temperature of interacting system is approximately presented by $T_i = \sqrt{\langle p_T^2 \rangle /2}$ [59–61], the lower panel shows the excitation function of initial temperature. Because of excluding different contribution fractions of the second component, the left panel [(a)(c)] shows some differences in the case of using two sets of parameter values. It should be noted that the root-mean square momentum component of particles in the rest frame of isotropic emission source is regarded as the initial temperature, or at the least it is a reflection of the initial temperature. The relations in the left panel are complex and multiple due to different sets of parameter values. The line in Figure 3b is fitted to various symbols by linear function

$$\langle p_T \rangle = (0.291 \pm 0.006) + (0.020 \pm 0.001) \ln \sqrt{s} \tag{11}$$

with $\chi^2/\text{ndof} = 54/82$. From the line one can see that the behavior of $\langle p_T \rangle$. In particular, with the increase of $\ln \sqrt{s}$ and including the contribution of second component, $\langle p_T \rangle$ increases approximately linearly. As a comparison, the red asterisks (green triangles) in Figure 3 represent the results for AA

collisions, which are indirectly obtained according to the parameter values listed in Tables A1 and A2. One can see that the results for *AA* collisions are greater than those for *pp* collisions at around 10 GeV and above.

The quantities $\langle p_T \rangle$ and T_i are very important to understand the excitation degree of interacting system. As for the right panel in Figure 3 which is for the two-component, the incremental trend for $\langle p_T \rangle$ and T_i with the increase of $\sqrt{s}$ ($\sqrt{s_{NN}}$) is a natural result due to more energy deposition at higher energy. Although $\langle p_T \rangle$ and T_i are obtained from the parameter values listed in Tables 1 and 2 (A1 and A2), they are independent of fits or models. More investigations on the excitation functions of $\langle p_T \rangle$ and T_i are needed due to their importance.
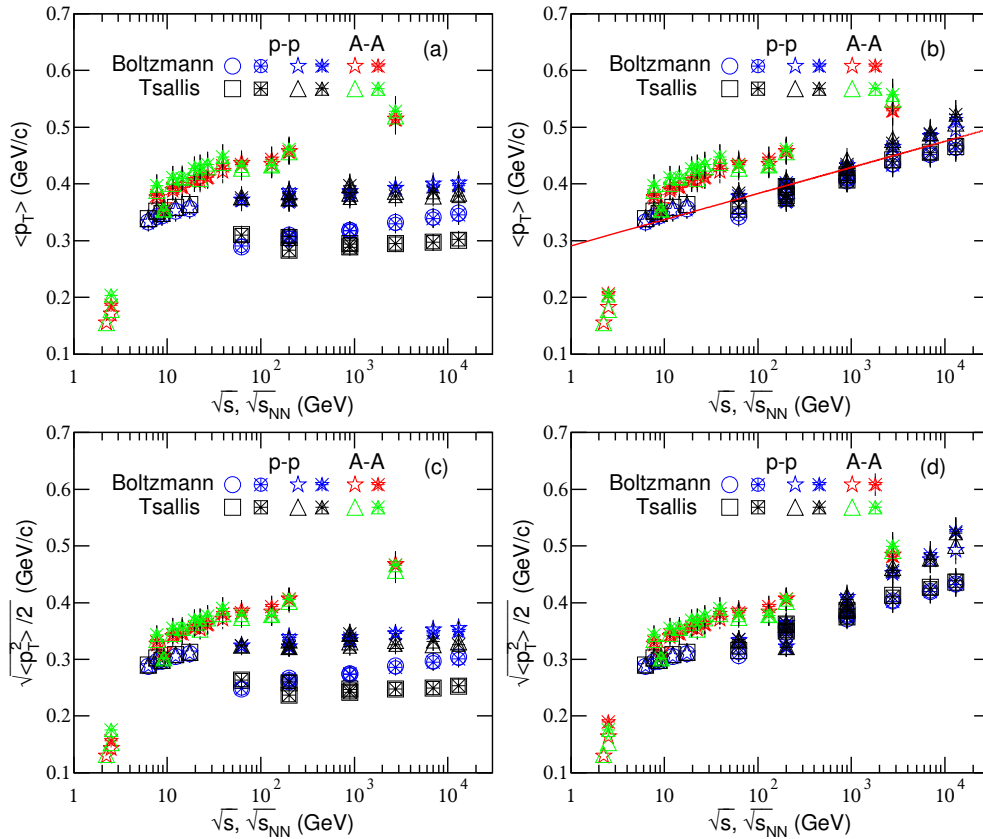
Figure 3. Excitation functions of (**a**,**b**) $\langle p_T \rangle$ and (**c**,**d**) $\sqrt{\langle p_T^2 \rangle / 2}$. The open symbols (open symbols with asterisks) represent the values corresponding to π^- (π^+) spectra. The blue circles (black squares) represent the results obtained indirectly from Equations (1) and (2) for the left panel, or from Equation (7) through Equations (1)–(3) for the right panel, by the first set of parameter values. The results by the second set of parameter values are presented by the blue asterisks (black triangles). These values are indirectly obtained according to the parameter values listed in Tables 1 and 2. The lines are the fitted results for various symbols for *pp* collisions. The red asterisks (green triangles) represent the results from *AA* collisions for comparisons, which are indirectly obtained according to the parameter values listed in Tables A1 and A2 in the Appendix A.

3.2. Comparison with Data by Equation (8)

To discuss further, for comparisons with the results from Equation (7), we reanalyze the spectra by Equation (8) and study the trends of new parameters. Figure 4 is the same as Figure 1, but showing the results fitted by Equation (8) through Equations (1) and (3) and through Equations (2) and (3) respectively. For Equation (8) through Equations (1) and (3), only one set of parameter values are used due to the fact that there is no correlation in the extraction of parameters in the two-component fit. For Equation (8) through Equations (2) and (3), two sets of parameter values are used to see the insensitivity of main parameters. The first set of parameter values are obtained by the method of least squares. The second set of parameter values are obtained by increasing or decreasing main parameters (T_0, β_T, q, and k) by a few percent, and limits the increase of χ^2 by a few percent. The values of related parameters are listed in Tables 3 and 4 which are the same as Tables 1 and 2 respectively, and with only one set of parameter values in Table 3. The related parameters are shown in Figure 5 and the leading-out parameters are shown in Figure 6, which are the same as Figures 2 and 3 respectively, and with only one set of parameter values for Equation (8) through Equations (1) and (3). In particular, k in Figure 5 is obtained by $k = \int_0^{p_1} A_1 f_S(p_T) dp_T$ due to $f_0(p_T)$ is normalized to 1, as discussed following Equation (8). The lines in Figure 6a,b are fitted by linear functions

$$\langle p_T \rangle = (0.318 \pm 0.004) + (0.010 \pm 0.001) \ln \sqrt{s} \qquad (12)$$

and

$$\langle p_T \rangle = (0.307 \pm 0.005) + (0.017 \pm 0.001) \ln \sqrt{s} \qquad (13)$$

with χ^2/ndof = 55/61 and 28/61 respectively, though the linear relationships between the parameters and $\ln \sqrt{s}$ may be not the best fitting functions. Similar to Figures 2 and 3, the results for AA collisions from Equation (8) are also presented in Figures 5 and 6 for comparisons. One can see the similarity in both pp and AA collisions in the considered energy range.

From Figure 4 one can see that Equation (8) fits similarly good the data as Equation (7). Because of the data being not available in very-low p_T range, Equation (10) is not used in the fit. T_0 and β_T in Figure 5 increase slightly from a few GeV to above 10 TeV with some fluctuations in some cases, which is partly similar to those in Figure 2. Other parameters in Figure 5 show somehow similar trends toFigure 2 with some differences. The left panels in Figures 3 and 6 are different due to the first component being in different superpositions. The right panels in Figures 3 and 6 are very similar to each other due to the same data sets being fitted. We would like to point out that Figures 1 and 4 present various cases which are displayed together and result in Figures 2 and 3 as well as Figures 5 and 6 depicting much more data in which some energy points are taken from Figures A1 and A2 in the Appendix A.

Table 3. Values of T_0, β_T, k, p_0, n, N_0, χ^2, and ndof corresponding to the solid (dotted) curves for π^- (π^+) spectra in Figure 4, where Equation (8) through Equations (1) and (3) is used.

Collab.	$\sqrt{s}$ (GeV)	Part.	T_0 (MeV)	β_T (c)	k	p_0 (GeV/c)	n	N_0	χ^2	ndof
NA61/	6.3	π^-	105 ± 5	0.31 ± 0.02	1	–	–	0.08 ± 0.01	24	15
SHINE	7.7	π^-	106 ± 5	0.32 ± 0.02	1	–	–	0.10 ± 0.01	44	15
INEL	8.8	π^-	107 ± 5	0.32 ± 0.02	1	–	–	0.10 ± 0.01	86	15
	12.3	π^-	108 ± 5	0.33 ± 0.02	1	–	–	0.12 ± 0.01	78	15
	17.3	π^-	109 ± 5	0.33 ± 0.02	1	–	–	0.13 ± 0.01	34	15
PHENIX	62.4	π^-	111 ± 5	0.35 ± 0.02	0.99 ± 0.01	3.58 ± 0.18	19.26 ± 0.56	19.48 ± 0.97	9	20
INEL		π^+	111 ± 5	0.35 ± 0.02	0.99 ± 0.01	3.59 ± 0.18	19.26 ± 0.56	19.54 ± 0.97	18	20
	200	π^-	115 ± 6	0.37 ± 0.02	0.99 ± 0.02	4.20 ± 0.21	18.71 ± 0.54	24.11 ± 1.20	16	21
		π^+	115 ± 6	0.36 ± 0.02	0.99 ± 0.02	4.31 ± 0.22	18.61 ± 0.53	24.96 ± 1.22	26	21
STAR	200	π^-	114 ± 6	0.34 ± 0.02	1	–	–	0.26 ± 0.01	2	6
NSD		π^+	114 ± 6	0.34 ± 0.02	1	–	–	0.27 ± 0.01	6	6
ALICE	900	π^-	118 ± 5	0.35 ± 0.02	0.95 ± 0.02	4.41 ± 0.22	18.67 ± 0.53	3.70 ± 0.18	101	27
INEL		π^+	118 ± 5	0.35 ± 0.02	0.95 ± 0.02	4.40 ± 0.22	18.67 ± 0.53	3.69 ± 0.18	131	27
CMS	900	π^-	118 ± 6	0.35 ± 0.02	0.91 ± 0.02	4.03 ± 0.20	18.87 ± 0.54	8.90 ± 0.44	47	16
INEL		π^+	118 ± 5	0.35 ± 0.02	0.91 ± 0.02	4.00 ± 0.20	18.67 ± 0.55	9.03 ± 0.45	43	16
	2760	π^-	122 ± 6	0.36 ± 0.02	0.89 ± 0.02	4.01 ± 0.18	18.80 ± 0.54	11.34 ± 0.57	57	16
		π^+	122 ± 6	0.37 ± 0.02	0.89 ± 0.02	4.02 ± 0.18	18.57 ± 0.53	11.54 ± 0.58	76	16
	7000	π^-	123 ± 6	0.38 ± 0.02	0.87 ± 0.02	4.03 ± 0.18	18.50 ± 0.52	14.50 ± 0.73	73	16
		π^+	123 ± 6	0.38 ± 0.02	0.86 ± 0.02	4.03 ± 0.18	18.40 ± 0.52	14.66 ± 0.73	90	16
	13000	π^-	126 ± 6	0.37 ± 0.02	0.83 ± 0.02	4.04 ± 0.19	18.30 ± 0.51	13.62 ± 0.68	31	16
		π^+	126 ± 6	0.37 ± 0.02	0.83 ± 0.02	4.04 ± 0.19	18.30 ± 0.51	13.84 ± 0.69	57	16

Table 4. Values of T_0, β_T, q, k, p_0, n, N_0, χ^2, and ndof corresponding to the dashed (dot-dashed) curves for π^- (π^+) spectra in Figure 4, where Equation (8) through Equations (2) and (3) is used.

| Collab.	$\sqrt{s}$ (GeV)	Part.	T_0 (MeV)	β_T (c)	q	k	p_0 (GeV/c)	n	N_0	χ^2	ndof
NA61/	6.3	π^-	83 ± 5	0.24 ± 0.01	1.04 ± 0.01	1	−	−	0.09 ± 0.01	11	14
SHINE	7.7	π^-	84 ± 5	0.25 ± 0.02	1.04 ± 0.01	1	−	−	0.10 ± 0.01	8	14
INEL	8.8	π^-	84 ± 5	0.25 ± 0.01	1.04 ± 0.01	1	−	−	0.10 ± 0.01	23	14
	12.3	π^-	85 ± 5	0.26 ± 0.01	1.05 ± 0.01	1	−	−	0.12 ± 0.01	11	14
	17.3	π^-	86 ± 5	0.26 ± 0.01	1.05 ± 0.01	1	−	−	0.13 ± 0.01	4	14
PHENIX	62.4	π^-	$82 \pm 4/88 \pm 4$	$0.24 \pm 0.01/0.27 \pm 0.01$	$1.07 \pm 0.01/1.05 \pm 0.01$	$0.99 \pm 0.01/0.99 \pm 0.01$	$3.20 \pm 0.19/3.19 \pm 0.18$	$18.56 \pm 0.51/18.56 \pm 0.51$	$18.27 \pm 0.91/19.18 \pm 0.93$	33/39	18
INEL		π^+	$82 \pm 5/88 \pm 4$	$0.24 \pm 0.01/0.27 \pm 0.01$	$1.07 \pm 0.01/1.06 \pm 0.01$	$0.99 \pm 0.01/0.99 \pm 0.01$	$3.20 \pm 0.19/3.21 \pm 0.18$	$18.56 \pm 0.51/18.56 \pm 0.51$	$17.19 \pm 0.89/17.36 \pm 0.90$	15/15	18
	200	π^-	$83 \pm 5/90 \pm 4$	$0.25 \pm 0.02/0.28 \pm 0.01$	$1.07 \pm 0.01/1.06 \pm 0.01$	$0.99 \pm 0.01/0.99 \pm 0.01$	$3.99 \pm 0.19/3.89 \pm 0.19$	$18.06 \pm 0.51/18.06 \pm 0.51$	$23.21 \pm 1.15/22.40 \pm 1.10$	16/31	19
		π^+	$83 \pm 5/90 \pm 4$	$0.25 \pm 0.02/0.28 \pm 0.01$	$1.07 \pm 0.01/1.06 \pm 0.01$	$0.99 \pm 0.01/0.99 \pm 0.01$	$4.09 \pm 0.20/4.09 \pm 0.20$	$18.01 \pm 0.50/18.01 \pm 0.51$	$23.00 \pm 1.16/22.40 \pm 1.14$	26/32	19
STAR	200	π^-	$83 \pm 5/89 \pm 4$	$0.25 \pm 0.01/0.28 \pm 0.01$	$1.06 \pm 0.01/1.04 \pm 0.01$	1	−	−	0.26 ± 0.01	34	5
NSD		π^+	$83 \pm 5/89 \pm 4$	$0.25 \pm 0.01/0.28 \pm 0.01$	$1.06 \pm 0.01/1.04 \pm 0.01$	1	−	−	0.26 ± 0.01	38	5
ALICE	900	π^-	$84 \pm 5/91 \pm 4$	$0.26 \pm 0.01/0.30 \pm 0.01$	$1.06 \pm 0.01/1.03 \pm 0.01$	$0.94 \pm 0.02/0.94 \pm 0.02$	$4.11 \pm 0.19/4.11 \pm 0.19$	$17.99 \pm 0.50/17.99 \pm 0.50$	$0.59 \pm 0.02/0.58 \pm 0.02$	187/287	25
INEL		π^+	$85 \pm 4/91 \pm 4$	$0.26 \pm 0.01/0.30 \pm 0.01$	$1.06 \pm 0.01/1.03 \pm 0.01$	$0.94 \pm 0.02/0.94 \pm 0.02$	$4.11 \pm 0.20/4.11 \pm 0.20$	$17.99 \pm 0.40/17.99 \pm 0.40$	$0.59 \pm 0.02/0.58 \pm 0.02$	232/333	25
CMS	900	π^-	$87 \pm 4/92 \pm 4$	$0.27 \pm 0.01/0.30 \pm 0.01$	$1.05 \pm 0.01/1.03 \pm 0.01$	$0.88 \pm 0.02/0.87 \pm 0.02$	$3.85 \pm 0.19/3.85 \pm 0.19$	$18.40 \pm 0.51/18.40 \pm 0.51$	$1.43 \pm 0.26/1.42 \pm 0.27$	79/95	14
INEL		π^+	$87 \pm 4/93 \pm 4$	$0.27 \pm 0.01/0.30 \pm 0.01$	$1.05 \pm 0.01/1.03 \pm 0.01$	$0.88 \pm 0.02/0.86 \pm 0.02$	$3.82 \pm 0.19/3.82 \pm 0.19$	$18.53 \pm 0.51/18.53 \pm 0.51$	$1.42 \pm 0.25/1.42 \pm 0.24$	70/72	14
	2760	π^-	$91 \pm 5/93 \pm 5$	$0.30 \pm 0.01/0.30 \pm 0.02$	$1.04 \pm 0.01/1.03 \pm 0.01$	$0.83 \pm 0.02/0.83 \pm 0.02$	$3.92 \pm 0.20/3.92 \pm 0.20$	$18.43 \pm 0.52/18.43 \pm 0.52$	$1.67 \pm 0.27/1.81 \pm 0.27$	70/72	14
		π^+	$92 \pm 5/93 \pm 5$	$0.30 \pm 0.02/0.30 \pm 0.02$	$1.04 \pm 0.01/1.03 \pm 0.01$	$0.84 \pm 0.02/0.84 \pm 0.02$	$3.92 \pm 0.20/3.92 \pm 0.20$	$18.43 \pm 0.51/18.43 \pm 0.51$	$1.83 \pm 0.27/1.82 \pm 0.26$	87/88	14
	7000	π^-	$92 \pm 4/94 \pm 5$	$0.30 \pm 0.02/0.31 \pm 0.02$	$1.04 \pm 0.01/1.03 \pm 0.01$	$0.79 \pm 0.02/0.81 \pm 0.02$	$3.94 \pm 0.19/3.94 \pm 0.19$	$18.41 \pm 0.50/18.41 \pm 0.50$	$2.30 \pm 0.32/2.30 \pm 0.33$	68/69	14
		π^+	$91 \pm 4/94 \pm 5$	$0.30 \pm 0.01/0.31 \pm 0.02$	$1.03 \pm 0.01/1.03 \pm 0.01$	$0.79 \pm 0.02/0.81 \pm 0.02$	$3.95 \pm 0.20/3.95 \pm 0.20$	$18.41 \pm 0.50/18.41 \pm 0.50$	$2.31 \pm 0.33/2.30 \pm 0.32$	87/92	14
	13000	π^-	$91 \pm 5/95 \pm 5$	$0.30 \pm 0.01/0.31 \pm 0.02$	$1.04 \pm 0.01/1.02 \pm 0.01$	$0.81 \pm 0.02/0.80 \pm 0.02$	$3.96 \pm 0.19/3.96 \pm 0.19$	$18.31 \pm 0.41/18.31 \pm 0.41$	$2.19 \pm 0.39/2.17 \pm 0.38$	34/39	14
		π^+	$91 \pm 5/95 \pm 5$	$0.30 \pm 0.01/0.31 \pm 0.02$	$1.03 \pm 0.01/1.02 \pm 0.01$	$0.78 \pm 0.02/0.79 \pm 0.02$	$3.96 \pm 0.19/3.96 \pm 0.19$	$18.31 \pm 0.41/18.31 \pm 0.41$	$2.18 \pm 0.38/2.17 \pm 0.36$	56/59	14
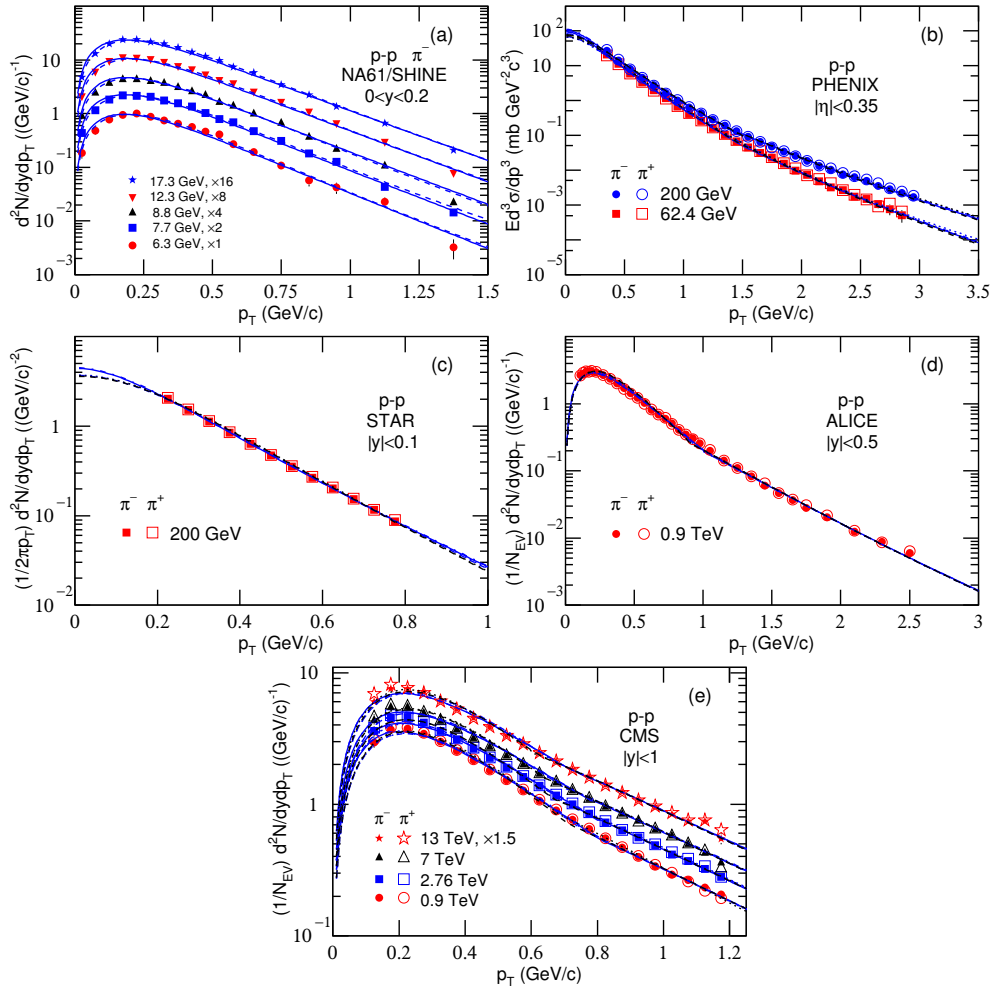
Figure 4. Same as Figure 1, but showing the results fitted by Equation (8) through Equations (1) and (3) with one set of parameter values and by Equation (8) through Equations (2) and (3) with two sets of parameter values. The blue solid (dotted) curves are the results for π^- (π^+) spectra fitted by Equation (8) through Equations (1) and (3), and the blue and black dashed (dot-dashed) curves are the results for π^- (π^+) spectra fitted by Equation (8) through Equations (2) and (3).
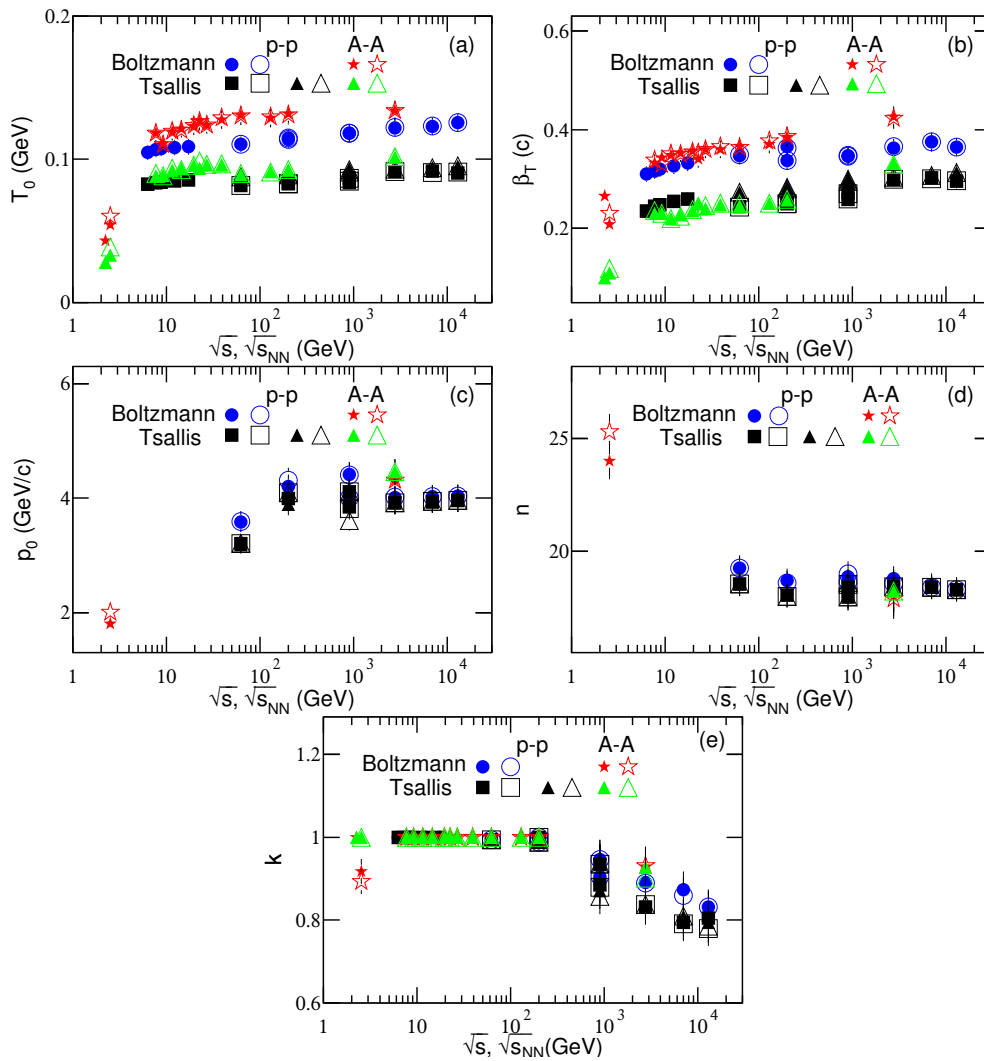
Figure 5. Same as Figure 2, but showing the results obtained from Equation (8) through Equations (1) and (3) with one set of parameter values and from Equation (8) through Equations (2) and (3) with two sets of parameter values. The blue circles represent the parameter values obtained from Equation (8) through Equations (1) and (3). black The squares (triangles) represent the first (second) set of parameter values obtained from Equation (8) through Equations (2) and (3). The related parameter values are listed in Tables 3 and 4. The red asterisks (green triangles) represent the parameter values from *AA* collisions for comparisons, which are listed in Tables A3 and A4 in the Appendix A.
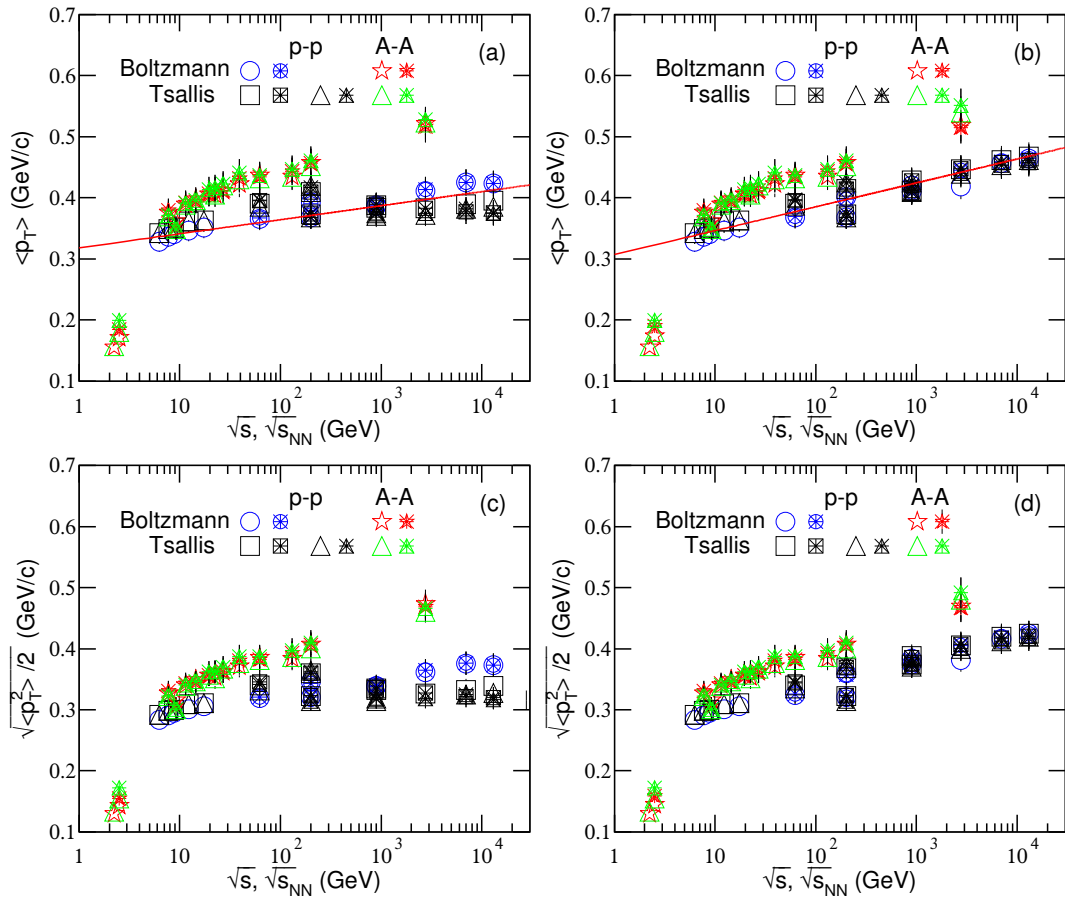
Figure 6. Same as Figure 3, but showing the results obtained from Equations (1) and (2) for the left panel, or from Equation (8) through Equations (1)–(3) for the right panel. The circles represent the results obtained indirectly from Equation (1) for the left panel, or from Equation (8) through Equations (1) and (3) for the right panel, by the parameter values. The squares (triangles) represent the results obtained indirectly from Equation (2) for the left panel, or from Equation (8) through Equations (2) and (3) for the right panel, by the first (second) set of parameter values. These values are indirectly obtained according to the parameter values listed in Tables 3 and 4. The red asterisks (green triangles) represent the results from AA collisions for comparisons, which are indirectly obtained according to the parameter values listed in Tables A3 and A4 in the Appendix A.

Before continuing this work, we would like to point out the justification and correctness for the comparisons of pp and central AA collisions in Figures 2, 3, 5 and 6. No matter peripheral or central AA collisions, a set of nucleon-nucleon collisions in participant region are similar to the minimum-bias pp collisions. Peripheral AA collisions are similar to central collisions with smaller projectile and target nuclei, while central AA collisions are just central collisions with large nuclei. Because of collision energies considered in this work are high, the nucleon-nucleon correlation, cluster structure, medium effect, and other nuclear effects in participant region can be neglected. Meanwhile, the cold nuclear or spectator effect in non-central AA collisions can be neglected, too. In our opinion, we may compare the minimum-bias pp collisions with the AA collisions in any centrality class.

Combining with our recent work [62], it is shown the similarity in pp and AA collisions, though AA collisions appear larger T_0, β_T, $\langle p_T \rangle$, and T_i in most cases. Moreover, it is well seen that Tsallis does not distinguish well between the data in pp and AA collisions [63–65]. Indeed, at high energy, both pp and AA collisions produce many particles and obey statistical law. In addition, pp collisions are the basic sub-process in AA collisions. It is natural that pp and AA collisions show similar law. However, concerning around 10–20 GeV change, this is expected as soon as QCD effects/calculations may not be directly applicable below this point, plus seem to be smoothed away by other processes in AA

collisions. This is well visible as a clear difference as shown in [63–65], where the data in pp collisions goes well with the data in electron-positron collisions, while the data in AA collisions are different.

The differences between Equations (7) and (8) are obviously, though the similar components are used in them. In our recent works [18,66], Equations (7) and (8) are used respectively. Although there is correlation in the extraction of parameters, a smooth curve can be easily obtained by Equation (7). Although it is not easy to obtain a smooth curve at the point of junction, there is no or less correlation in the extraction of parameters by Equation (8). In consideration of obtaining a set of parameters with least correlation, we are inclined to use Equation (8) to extract the related parameters. This inclining results in Equation (8) to separate determinedly the contributions of soft and hard processes.

It should be noted that the system of pp collisions at low energy is probably not in thermal equilibrium or local thermal equilibriums due to low multiplicity, which is not the case of the present work. In fact, the present work treats pp collisions at high energies in which the multiplicities in most cases are not too low. In addition, related review work [67] shows that small system also appears similar collective behavior to AA collisions. This renders that the idea of local thermal equilibrium is suitable to high energy pp collisions for which the blast-wave fit can be used, though QGP is not expected to form in minimum-bias events.

Although we have used the blast-wave fit in the superposition function with two components in which the second component is an inverse power-law, the blast-wave part is not necessary for fitting process itself. In fact, the superposition of (two-)Boltzmann (or Tsallis) distribution and inverse power-law can fit the data in most cases [30,31,65]. In particular, in our very recent work [68], we used the Tsallis–Pareto-type function [28,69,70] to fit p_T spectra in a wide range, in which there is no boosted part. The merits of the boosted part are that some additional quantities such as T_0 and β_T can be obtained and physics picture is more abundant.

To avoid the dependences of T_0 and β_T on fits or models, one can use $\langle p_T \rangle$ to describe synchronously T_0 and β_T. Generally, $\langle p_T \rangle$ is independent of fits or models, though it can be calculated from fits or models. Averagely, the contribution of one participant in each binary collisions is $\langle p_T \rangle / 2$ which is resulted from both the thermal motion and flow effect. Let k_0 denote the contribution fraction of thermal motion. The contribution fraction of flow effect is naturally $1 - k_0$. Thus, we define $T_0 = k_0 \langle p_T \rangle / 2$ and $\beta_T = (1 - k_0) \langle p_T \rangle / 2 m_0 \overline{\gamma}$. As a free parameter, k_0 depends on collision energy, which is needed to study further.

3.3. More Discussions

Before summary and conclusions, we would like to underline the preponderance of the present work. Comparing with PYTHIA or other perturbative QCD simulation tools [71–74], the present work is simpler and more applicative in obtaining the excitation functions of T_0 and β_T, though the usual fitting method is used. In a recent work [75], it was pointed out that the PYTHIA Monte Carlo [71,72] disagrees with some data, and the two-component (soft+hard) model describes the data accurately and comprehensively, though the two-component model used in [75] is different from the fit used in the present work. In addition, the present work is a data-driven reanalysis based on some physics considerations, but not a simple fit to the data. From the data-driven reanalysis, the excitation functions of some quantities have been obtained.

From the excitation functions, one can see some complex structures which are useful to study the properties of particle production and system evolution at different energies. In particular, in the energy range around 10 GeV, the excitation functions have transition which implies the phase of interaction matter had changed. In addition, by using the two-component fit, the present work also presents a new method to extract the contribution fraction of hard component. One can see that this contribution fraction is 0 in the energy range around 10 GeV. This implies that the interactions in the energy range around 10 GeV have only soft component, and that above 10 GeV have both soft and hard components. The interaction mechanisms in the two energy ranges are different.

We would like to emphasize that the aim of the present work is to look for possible signatures of a transition from baryon-dominated to meson-dominated hadron production mechanism by fitting pion p_T spectra at mid-(pseudo)rapidity in pp collisions which also show collective phenomenon [67]. The main conclusion regards a possible indication of such an effect at about 10–20 GeV visible in a drop of the temperature extracted using a blast-wave model with Boltzmann distribution to model the soft excitation mode. Such a conclusion seems not straightforward since the results are strongly biased by different $p_{T\max}$ used to fit data at different energies. In fact, the results are less affected by $p_{T\max}$ due to the fact that the parameters are mainly determined by the spectra in low and intermediate p_T regions. Larger $p_{T\max}$ does not change the trend of inverse power-law, which does not affect obviously the parameters. Although $p_{T\max}$ has no obvious influence on the parameters, we have used $p_{T\max} = 5$ Gev/c in our calculation.

It should be noted that the blast-wave analysis is known to be sensitive to the selected p_T range in the case of using a not too wide and local one such as 1–2 GeV/c. To avoid this dependence, we have used a wide enough p_T range from 0 to a large value, but not a narrow and local one. In addition, looking at the fit results when using a Tsallis function to describe soft excitation processes such a drop in the k-parameter is no longer visible which seems to mean that the fit is less sensitive to the hard component and also less sensitive to $p_{T\max}$. Using the Tsallis function assumption also the drop in the temperature is no longer visible which means that the effect on the temperature seen with the Boltzmann assumption seems to be model dependent. In fact, the parameters discussed in the present work are indeed model dependent. We hope to extract model independent parameters in the near future. Our definition $T_0 = k_0 \langle p_T \rangle / 2$ and $\beta_T = (1 - k_0) \langle p_T \rangle / 2 m_0 \overline{\gamma}$ are a possible choice for the model independent parameters.

On the other hand, although comparing Boltzmann with Tsallis is an interesting physical problem, which could not be understood without another comparison with the generic super-statistics, as the one implemented in particle productions [76–79]. The latter—in contrary to Boltzmann and Tsallis—lets the system alone judge about its statistical nature, whether extensive or non-extensive (equilibrium or non-equilibrium). As pointed out in [76–79], the particle production at BES energies is likely a non-extensive process but not necessarily Boltzmann or Tsallis type. Indeed, further study on particle production in high energy collisions is needed in the future.

In particular, larger T_0 means higher excitation degree and shorter lifetime of the fireball formed in high energy collisions. At the LHC energy, the fireball should have higher excitation degree comparing with that at the top RHIC energy, though longer lifetime is possible at the LHC energy [55,80]. As a result of competition between excitation degree and lifetime, T_0 shows the trend of increase with energy in the present work. Meanwhile, our result on larger β_T means quicker expansion at the LHC energy. These trends are harmonious with those of $\langle p_T \rangle$ and T_i as well as other method such as the alternative method [16,18,66] by which T_0 and β_T are also obtained.

4. Summary and Conclusions

The transverse momentum spectra of π^- and π^+ produced at mid-(pseudo)rapidity in pp collisions over an energy range from a few GeV to above 10 TeV have been analyzed by the superposition of the blast-wave fit with Boltzmann distribution or with Tsallis distribution and the inverse power-law (Hagedorn function). The fit results are well fitting to the experimental data of NA61/SHINE, PHENIX, STAR, ALICE, and CMS Collaborations. The values of related parameters are extracted from the fit process and the excitation functions of parameters are obtained.

In the particular superposition Equation (7) and with a given selection, both excitation functions of T_0 and β_T obtained from the blast-wave fit with Boltzmann distribution show a hill at $\sqrt{s} \approx 10$ GeV, a drop at dozens of GeV, and an increase from dozens of GeV to above 10 TeV. The mentioned two excitation functions obtained from the blast-wave fit with Tsallis distribution does not show such a complex structure, but a very low hill. In another selection for the parameters in Equation (7) or in the superposition Equation (8), T_0 and β_T increase generally quickly from a few GeV to about 10 GeV

and then slightly at above 10 GeV. There is no the complex structure, too. In both superpositions, the excitation function of p_0 (n) shows a slight decrease (increase) in the case of the hard component being available. From the RHIC to LHC, there is a positive (negative) correlation between T_0 and β_T (p_0 and n). The contribution of hard component slightly increases from dozens of GeV to above 10 TeV, and it has no contribution at around 10 GeV.

In the case of considering the two components together, the mean transverse momentum and the initial temperature increase obviously with the increase of logarithmic collision energy in the considered energy range. From a few GeV to above 10 TeV, the collision system takes place possibly a transition at around 10 GeV, where the transition from a baryon-dominated to a meson-dominated final state takes place. No matter what a structure appears, the energy range around 10 GeV is a special one due to the slope of T_0 excitation function having large variation. Indeed, the mentioned energy range is needed further study in the future.

Conflicts of Interest: The authors declare that there are no conflicts of interest regarding the publication of this paper. The funding agencies have no role in the design of the study; in the collection, analysis, or interpretation of the data; in the writing of the manuscript, or in the decision to publish the results.

Data Availability: The data used to support the findings of this study are included within the article and are cited at relevant places within the text as references.

Compliance with Ethical Standards: The authors declare that they are in compliance with ethical standards regarding the content of this paper.

Appendix A. Fit Results from AA Collisions

Although our previous work [62] studied the excitation functions of T_0 and β_T in AA collisions, different fit functions were used there. To make a comparison with the results from pp collisions in the present work, we have to use the same fit functions, i.e., Equations (7) and (8), to re-fit the spectra from AA collisions.

Figure A1 shows the spectra of π^- and π^+ produced in mid-rapidity range in central Cu-Cu, Au-Au, and Pb-Pb collisions at high energies. Panels (a)–(f) represent the data by various symbols measured by the FOPI [81], STAR [55], STAR [7], PHENIX [82], STAR [6], and ALICE [20] Collaborations, respectively, where for 2.24 GeV Au-Au collisions in panel (a) only the spectrum of π^- is available. As the same as Figure 1, the solid (dotted) curves are our results for π^- (π^+) spectra fitted by Equation (7) through Equations (1) and (3), and the dashed (dot-dashed) curves are our results for π^- (π^+) spectra fitted by Equation (7) through Equations (2) and (3), where only one set of parameters is used. The values of parameters are listed in Tables A1 and A2 with χ^2 and ndof, where the values of parameters are used directly in Figure 2 and indirectly in Figure 3. The fit results based on Equation (7) are well fitting to the experimental data measured in central AA collisions by the international collaborations [6,7,20,55,81,82].

Figure A2 is the same as Figure A1, but it shows the fit results from Equation (8) through Equations (1) and (3) as well as through Equations (2) and (3). As the same as Figure 4, the solid (dotted) curves are the results for π^- (π^+) spectra from Equation (8) through Equations (1) and (3), and the dashed (dot-dashed) curves are the results for π^- (π^+) spectra from Equation (8) through Equations (2) and (3). The values of parameters are listed in Tables A3 and A4 with χ^2 and ndof, where

the values of parameters are used directly in Figure 5 and indirectly in Figure 6. The fit results based on Equation (8) are well fitting to the experimental data measured in central AA collisions by the international collaborations [6,7,20,55,81,82]. It should be noted that Tables A3 and A4 are nearly the same as Tables A1 and A2 respectively, if not equal in error. The reason is that narrow p_T ranges are used, in which the first component plays complete or main rule. The difference between Equations (7) and (8) is then not obvious.
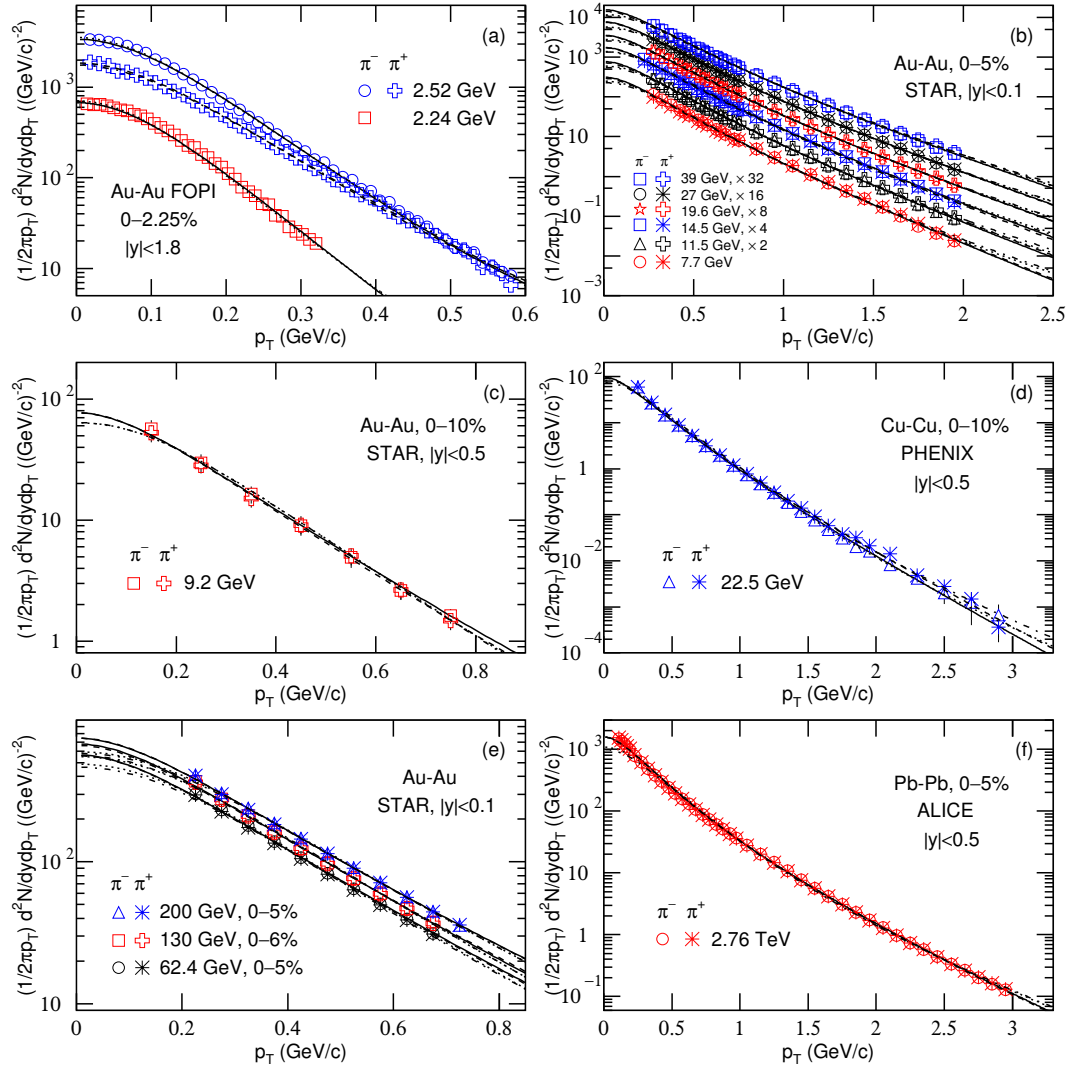

Figure A1. Same as Figure 1, but showing the results from central AA collisions. Panels (**a**–**f**) represent the data by various symbols measured by the FOPI [81], STAR [55], STAR [7], PHENIX [82], STAR [6], and ALICE [20] Collaborations, respectively.
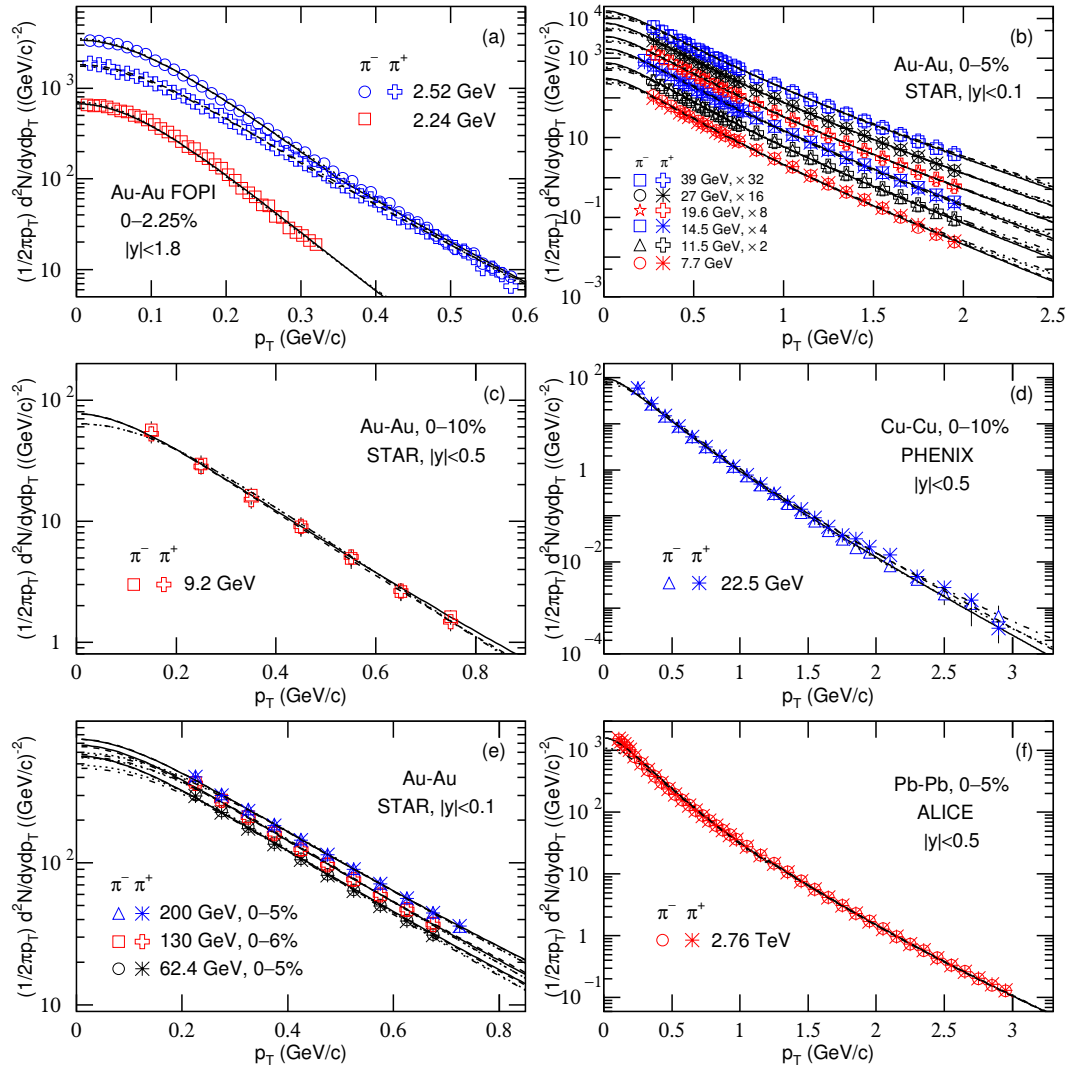
Figure A2. Same as Figures 4 and A1, but showing the results from central *AA* collisions and Equation (8).

Table A1. Values of T_0, β_T, k, p_0, n, N_0, χ^2, and ndof corresponding to the solid (dotted) curves for π^- (π^+) spectra in Figure A1.

Collab.	$\sqrt{s_{NN}}$ (GeV)	Part.	T_0 (MeV)	β_T (c)	k	p_0 (GeV/c)	n	N_0	χ^2	ndof
FOPI Au-Au	2.24	π^-	43 ± 2	0.27 ± 0.02	1	–	–	1734.50 ± 16.33	38	33
0–2.25%	2.52	π^-	54 ± 3	0.21 ± 0.02	0.96 ± 0.01	3.81 ± 0.23	19.00 ± 0.9	2180.50 ± 18.31	11	40
		π^+	59 ± 6	0.23 ± 0.02	0.94 ± 0.01	3.91 ± 0.31	18.00 ± 0.5	1385.40 ± 13.01	16	40
STAR Au-Au	7.7	π^-	118 ± 6	0.33 ± 0.01	1	–	–	20.08 ± 1.08	17	23
0–5%		π^+	118 ± 6	0.34 ± 0.01	1	–	–	19.03 ± 0.64	27	23
0–10%	9.2	π^-	111 ± 6	0.34 ± 0.02	1	–	–	21.18 ± 1.00	1	4
		π^+	110 ± 6	0.30 ± 0.02	1	–	–	21.68 ± 1.62	1	4
0–5%	11.5	π^-	119 ± 6	0.35 ± 0.02	1	–	–	25.76 ± 1.80	4	23
		π^+	120 ± 6	0.35 ± 0.02	1	–	–	24.39 ± 1.32	8	23
	14.5	π^-	121 ± 6	0.35 ± 0.02	1	–	–	30.22 ± 1.60	1	25
		π^+	120 ± 7	0.35 ± 0.02	1	–	–	29.47 ± 1.62	1	25
	19.6	π^-	123 ± 7	0.36 ± 0.02	1	–	–	31.62 ± 1.50	3	23
		π^+	124 ± 7	0.36 ± 0.02	1	–	–	31.10 ± 1.52	3	23
	27	π^-	124 ± 6	0.36 ± 0.02	1	–	–	34.95 ± 1.40	3	23
		π^+	124 ± 5	0.36 ± 0.02	1	–	–	34.31 ± 1.22	3	23
	39	π^-	128 ± 5	0.36 ± 0.02	1	–	–	37.09 ± 2.12	4	23
		π^+	129 ± 5	0.37 ± 0.02	1	–	–	35.06 ± 2.42	2	23
	62.4	π^-	131 ± 6	0.37 ± 0.02	1	–	–	42.60 ± 2.20	9	4
		π^+	130 ± 6	0.36 ± 0.02	1	–	–	42.16 ± 2.36	9	4
0–6%	130	π^-	129 ± 5	0.37 ± 0.02	1	–	–	50.22 ± 1.55	25	4
		π^+	130 ± 6	0.38 ± 0.02	1	–	–	48.88 ± 1.09	21	4
0–5%	200	π^-	132 ± 6	0.39 ± 0.02	1	–	–	57.94 ± 1.67	6	5
		π^+	131 ± 5	0.39 ± 0.02	1	–	–	57.81 ± 1.54	9	5
PHENIX Cu-Cu	22.5	π^-	127 ± 6	0.34 ± 0.02	1	–	–	35.06 ± 1.85	10	20
0–10%		π^+	126 ± 6	0.35 ± 0.02	1	–	–	34.93 ± 2.21	13	20
ALICE Pb-Pb	2760	π^-	133 ± 5	0.42 ± 0.02	0.94 ± 0.02	5.81 ± 0.34	18.00 ± 0.87	759.82 ± 12.22	37	35
0–5%		π^+	133 ± 6	0.43 ± 0.02	0.84 ± 0.02	5.79 ± 0.35	18.00 ± 0.87	754.17 ± 21.00	37	35

Table A2. Values of T_0, β_T, q, k, p_0, n, N_0, χ^2, and ndof corresponding to the dashed (dot-dashed) curves for π^- (π^+) spectra in Figure A1.

Collab.	$\sqrt{s_{NN}}$ (GeV)	Part.	T_0 (MeV)	β_T (c)	q	k	p_0 (GeV/c)	n	N_0	χ^2	ndof
FOPI Au-Au	2.24	π^-	28 ± 2	0.10 ± 0.02	1.07 ± 0.01	1	−	−	1734.50 ± 15.01	42	32
0-2.25%	2.52	π^-	33 ± 2	0.11 ± 0.02	1.08 ± 0.01	1	−	−	2205.40 ± 18.01	5	42
		π^+	39 ± 3	0.12 ± 0.02	1.08 ± 0.01	1	−	−	1362.80 ± 12.01	13	42
STAR Au-Au	7.7	π^-	88 ± 6	0.23 ± 0.01	1.06 ± 0.01	1	−	−	19.45 ± 1.08	31	22
0–5%		π^+	90 ± 6	0.24 ± 0.01	1.06 ± 0.01	1	−	−	18.64 ± 0.64	35	22
0–10%	9.2	π^-	89 ± 6	0.23 ± 0.02	1.04 ± 0.01	1	−	−	21.99 ± 1.00	2	3
		π^+	88 ± 6	0.23 ± 0.02	1.04 ± 0.01	1	−	−	21.93 ± 1.62	2	3
0–5%	11.5	π^-	92 ± 6	0.22 ± 0.02	1.06 ± 0.01	1	−	−	25.13 ± 1.80	18	22
		π^+	94 ± 5	0.22 ± 0.02	1.06 ± 0.02	1	−	−	24.27 ± 1.22	21	22
	14.5	π^-	93 ± 5	0.23 ± 0.02	1.06 ± 0.02	1	−	−	30.47 ± 1.20	3	24
		π^+	93 ± 5	0.23 ± 0.02	1.06 ± 0.01	1	−	−	29.47 ± 2.22	3	24
	19.6	π^-	96 ± 6	0.24 ± 0.02	1.06 ± 0.01	1	−	−	32.12 ± 1.30	26	22
		π^+	96 ± 5	0.24 ± 0.02	1.06 ± 0.01	1	−	−	30.47 ± 1.22	10	22
	27	π^-	96 ± 6	0.24 ± 0.02	1.06 ± 0.02	1	−	−	34.32 ± 2.10	17	22
		π^+	97 ± 5	0.25 ± 0.02	1.06 ± 0.01	1	−	−	32.79 ± 1.52	9	22
	39	π^-	96 ± 5	0.25 ± 0.02	1.06 ± 0.02	1	−	−	35.59 ± 1.42	15	22
		π^+	97 ± 5	0.25 ± 0.02	1.07 ± 0.02	1	−	−	34.18 ± 1.22	8	22
	62.4	π^-	89 ± 7	0.25 ± 0.02	1.07 ± 0.01	1	−	−	41.66 ± 1.20	16	3
		π^+	90 ± 7	0.25 ± 0.02	1.07 ± 0.02	1	−	−	40.28 ± 1.62	14	3
0–6%	130	π^-	91 ± 7	0.25 ± 0.02	1.07 ± 0.01	1	−	−	48.57 ± 1.90	57	3
		π^+	91 ± 5	0.25 ± 0.02	1.07 ± 0.01	1	−	−	49.00 ± 1.02	49	3
0–5%	200	π^-	93 ± 7	0.26 ± 0.02	1.08 ± 0.01	1	−	−	55.93 ± 1.60	20	4
		π^+	93 ± 5	0.26 ± 0.02	1.08 ± 0.01	1	−	−	55.10 ± 1.52	18	4
PHENIX Cu-Cu	22.5	π^-	94 ± 6	0.25 ± 0.02	1.05 ± 0.01	1	−	−	36.63 ± 2.62	8	19
0–10%		π^+	99 ± 6	0.25 ± 0.02	1.06 ± 0.01	1	−	−	35.94 ± 3.65	21	19
ALICE Pb-Pb	2760	π^-	101 ± 5	0.33 ± 0.02	1.07 ± 0.02	0.90 ± 0.02	6.16 ± 0.34	17.93 ± 0.87	715.84 ± 21.33	88	34
0–5%		π^+	102 ± 6	0.33 ± 0.02	1.07 ± 0.02	0.91 ± 0.02	6.26 ± 0.35	17.63 ± 0.87	671.86 ± 13.56	73	34

Table A3. Values of T_0, β_T, k, p_0, n, N_0, χ^2, and ndof corresponding to the solid (dotted) curves for π^- (π^+) spectra in Figure A2.

Collab.	$\sqrt{s_{NN}}$ (GeV)	Part.	T_0 (MeV)	β_T (c)	k	p_0 (GeV/c)	n	N_0	χ^2	ndof
FOPI Au-Au	2.24	π^-	43 ± 2	0.27 ± 0.01	1	–	–	1734.50 ± 15.01	38	33
0–2.25%	2.52	π^-	54 ± 3	0.21 ± 0.01	0.96 ± 0.01	3.81 ± 0.16	19.00 ± 1.19	2180.50 ± 22.01	11	39
		π^+	59 ± 3	0.23 ± 0.01	0.94 ± 0.01	3.91 ± 0.26	18.00 ± 1.25	1385.40 ± 33.01	16	39
STAR Au-Au	7.7	π^-	118 ± 5	0.33 ± 0.01	1	–	–	20.08 ± 1.68	17	23
0–5%		π^+	118 ± 5	0.34 ± 0.01	1	–	–	19.03 ± 1.84	27	23
0–10%	9.2	π^-	111 ± 4	0.34 ± 0.02	1	–	–	21.18 ± 1.60	1	4
		π^+	110 ± 5	0.30 ± 0.01	1	–	–	21.68 ± 1.62	1	4
0–5%	11.5	π^-	119 ± 6	0.35 ± 0.02	1	–	–	25.76 ± 1.45	4	23
		π^+	120 ± 6	0.35 ± 0.02	1	–	–	24.39 ± 1.22	8	23
	14.5	π^-	121 ± 5	0.35 ± 0.02	1	–	–	30.22 ± 1.30	1	25
		π^+	120 ± 6	0.35 ± 0.01	1	–	–	29.47 ± 1.02	1	25
	19.6	π^-	123 ± 6	0.36 ± 0.01	1	–	–	31.62 ± 1.15	3	23
		π^+	124 ± 5	0.36 ± 0.01	1	–	–	31.10 ± 1.53	3	23
	27	π^-	124 ± 6	0.36 ± 0.02	1	–	–	34.95 ± 1.80	3	23
		π^+	124 ± 5	0.36 ± 0.01	1	–	–	34.31 ± 1.82	3	23
	39	π^-	128 ± 7	0.36 ± 0.01	1	–	–	37.09 ± 1.22	4	23
		π^+	129 ± 5	0.37 ± 0.01	1	–	–	35.06 ± 1.32	2	23
	62.4	π^-	131 ± 5	0.37 ± 0.02	1	–	–	42.60 ± 1.70	9	4
		π^+	130 ± 6	0.36 ± 0.02	1	–	–	42.16 ± 1.52	9	4
0–6%	130	π^-	129 ± 6	0.37 ± 0.01	1	–	–	50.22 ± 1.60	25	4
		π^+	130 ± 6	0.38 ± 0.01	1	–	–	48.88 ± 1.02	21	4
0–5%	200	π^-	132 ± 5	0.39 ± 0.01	1	–	–	57.94 ± 2.20	6	5
		π^+	131 ± 5	0.39 ± 0.02	1	–	–	57.81 ± 2.22	9	5
PHENIX Cu-Cu	22.5	π^-	127 ± 6	0.34 ± 0.02	1	–	–	35.06 ± 1.01	10	20
0–10%		π^+	126 ± 6	0.35 ± 0.02	1	–	–	34.93 ± 1.01	13	20
ALICE Pb-Pb	2760	π^-	133 ± 5	0.42 ± 0.02	0.94 ± 0.02	5.81 ± 0.34	18.00 ± 0.87	759.82 ± 14.07	37	35
0–5%		π^+	133 ± 6	0.43 ± 0.02	0.84 ± 0.02	5.79 ± 0.35	18.00 ± 0.87	754.17 ± 13.07	37	35

Table A4. Values of T_0, β_T, q, k, p_0, n, N_0, χ^2, and ndof corresponding to the dashed (dot-dashed) curves for π^- (π^+) spectra in Figure A2.

Collab.	$\sqrt{s_{NN}}$ (GeV)	Part.	T_0 (MeV)	β_T (c)	q	k	p_0 (GeV/c)	n	N_0	χ^2	ndof
FOPI Au-Au	2.24	π^-	28 ± 2	0.10 ± 0.02	1.07 ± 0.01	1	−	−	1734.50 ± 20.31	42	32
0–2.25%	2.52	π^-	33 ± 3	0.11 ± 0.02	1.08 ± 0.01	1	−	−	2205.40 ± 18.12	5	42
		π^+	39 ± 3	0.12 ± 0.02	1.08 ± 0.01	1	−	−	1362.80 ± 13.22	13	42
STAR Au-Au	7.7	π^-	88 ± 6	0.23 ± 0.01	1.06 ± 0.01	1	−	−	19.45 ± 1.58	31	22
0–5%		π^+	90 ± 5	0.24 ± 0.01	1.06 ± 0.01	1	−	−	18.64 ± 1.34	35	22
0–10%	9.2	π^-	89 ± 6	0.23 ± 0.01	1.04 ± 0.01	1	−	−	21.99 ± 1.51	2	3
		π^+	88 ± 6	0.23 ± 0.02	1.04 ± 0.01	1	−	−	21.93 ± 2.02	2	3
0–5%	11.5	π^-	92 ± 6	0.22 ± 0.01	1.06 ± 0.01	1	−	−	25.13 ± 1.20	18	22
		π^+	94 ± 5	0.22 ± 0.02	1.06 ± 0.01	1	−	−	24.27 ± 1.56	21	22
	14.5	π^-	93 ± 5	0.23 ± 0.01	1.06 ± 0.01	1	−	−	30.47 ± 1.30	3	24
		π^+	93 ± 5	0.23 ± 0.02	1.06 ± 0.01	1	−	−	29.47 ± 1.72	3	24
	19.6	π^-	96 ± 5	0.24 ± 0.02	1.06 ± 0.02	1	−	−	32.12 ± 1.20	26	22
		π^+	96 ± 7	0.24 ± 0.02	1.06 ± 0.02	1	−	−	30.47 ± 1.51	10	22
	27	π^-	96 ± 7	0.24 ± 0.02	1.06 ± 0.02	1	−	−	34.32 ± 1.36	17	22
		π^+	97 ± 7	0.25 ± 0.01	1.06 ± 0.02	1	−	−	32.79 ± 1.28	9	22
	39	π^-	96 ± 7	0.25 ± 0.01	1.06 ± 0.01	1	−	−	35.59 ± 1.51	15	22
		π^+	97 ± 5	0.25 ± 0.02	1.07 ± 0.01	1	−	−	34.18 ± 1.42	8	22
	62.4	π^-	89 ± 5	0.25 ± 0.02	1.07 ± 0.02	1	−	−	41.66 ± 1.33	16	3
		π^+	90 ± 6	0.25 ± 0.01	1.07 ± 0.01	1	−	−	40.28 ± 1.12	14	3
0–6%	130	π^-	91 ± 6	0.25 ± 0.02	1.07 ± 0.01	1	−	−	48.57 ± 1.66	57	3
		π^+	91 ± 5	0.25 ± 0.01	1.07 ± 0.01	1	−	−	49.00 ± 1.42	49	3
0–5%	200	π^-	93 ± 6	0.26 ± 0.02	1.08 ± 0.02	1	−	−	55.93 ± 1.70	20	4
		π^+	93 ± 5	0.26 ± 0.02	1.08 ± 0.01	1	−	−	55.10 ± 2.02	18	4
PHENIX Cu-Cu	22.5	π^-	94 ± 6	0.25 ± 0.01	1.05 ± 0.02	1	−	−	36.63 ± 2.66	8	19
0–10%		π^+	99 ± 6	0.25 ± 0.01	1.06 ± 0.02	1	−	−	35.94 ± 1.22	21	19
ALICE Pb-Pb	2760	π^-	101 ± 5	0.33 ± 0.01	1.07 ± 0.01	0.90 ± 0.02	6.16 ± 0.34	17.93 ± 0.87	715.84 ± 11.39	88	34
0–5%		π^+	102 ± 6	0.33 ± 0.02	1.07 ± 0.02	0.91 ± 0.02	6.26 ± 0.35	17.63 ± 0.87	671.86 ± 16.22	73	34

References

1. Cleymans, J.; Oeschler, H.; Redlich, K.; Wheaton, S. Comparison of chemical freeze-out criteria in heavy-ion collisions. *Phys. Rev. C* **2006**, *73*, 034905.

2. Andronic, A.; Braun-Munzinger, P.; Stachel, J. Thermal hadron production in relativistic nuclear collisions. *Acta Phys. Pol. B* **2009**, *40*, 1005–1012.

3. Andronic, A.; Braun-Munzinger, P.; Stachel, J. The horn, the hadron mass spectrum and the QCD phase diagram: The statistical model of hadron production in central nucleus-nucleus collisions. *Nucl. Phys. A* **2010**, *834*, 237c–240c.

4. Hama, Y.; Navarra, F.S. Energy and mass number dependence of the dissociation temperature in hydrodynamical models. *Z. Phys. C* **1992** , *53*, 501–506.

5. Schnedermann, E.; Sollfrank, J.; Heinz, U. Thermal phenomenology of hadrons from 200A GeV S + S collisions. *Phys. Rev. C* **1993**, *48*, 2462–2475.

6. Abelev, B.I.; STAR Collaboration. Systematic measurements of identified particle spectra in pp, $d + $ Au, and Au + Au collisions at the STAR detector. *Phys. Rev. C* **2009**, *79*, 034909.

7. Abelev, B.I.; STAR Collaboration. Identified particle production, azimuthal anisotropy, and interferometry measurements in Au+Au collisions at $\sqrt{s_{NN}} = 9.2$ GeV. *Phys. Rev. C* **2010**, *81*, 024911.

8. Tang, Z.B.; Xu, Y.C.; Ruan, L.J.; Van Buren, G.; Wang, F.Q.; Xu, Z.B. Spectra and radial flow at RHIC with Tsallis statistics in a blast-wave description. *Phys. Rev. C* **2009**, *79*, 051901(R).

9. Tang, Z.B.; Li, Y.; Ruan, L.J.; Shao, M.; Chen, H.F.; Li, C.; Mohanty, B.; Sorensen, P.; Tang, A.H.; Xu, Z.B. Statistical origin of constituent-quark scaling in the QGP hadronization. *Chin. Phys. Lett.* **2013**, *30*, 031201.

10. Jiang, K.; Zhu, Y.Y.; Liu, W.T.; Chen, H.F.; Li, C.; Ruan, L.J.; Tang, Z.B.; Xu, Z.B. Onset of radial flow in p+p collisions. *Phys. Rev. C* **2015**, *91*, 024910.

11. Takeuchi, S.; Murase, K.; Hirano, T.; Huovinen, P.; Nara, Y. Effects of hadronic rescattering on multistrange hadrons in high-energy nuclear collisions. *Phys. Rev. C* **2015**, *92*, 044907.

12. Heiselberg, H.; Levy, A.M. Elliptic flow and HBT in noncentral nuclear collisions. *Phys. Rev. C* **1999**, *59*, 2716–2727.

13. Heinz, U.W. Concepts of heavy-ion physics. *arXiv* **2003**, arXiv:hep-ph/0407360.

14. Russo, R. Measurement of D^+ Meson Production in p-Pb Collisions with the ALICE Detector. Ph.D. Thesis, Universita degli Studi di Torino, Torino, Italy, 2015.

15. Wei, H.-R.; Liu, F.-H.; Lacey, R.A. Kinetic freeze-out temperature and flow velocity extracted from transverse momentum spectra of final-state light flavor particles produced in collisions at RHIC and LHC. *Eur. Phys. J. A* **2016**, *A52*, 102.

16. Lao, H.-L.; Wei, H.-R.; Liu, F.-H.; Lacey, R.A. An evidence of mass-dependent differential kinetic freeze-out scenario observed in Pb-Pb collisions at 2.76 TeV. *Eur. Phys. J. A* **2016**, *52*, 203.

17. Wei, H.-R.; Liu, F.-H.; Lacey, R.A. Disentangling random thermal motion of particles and collective expansion of source from transverse momentum spectra in high energy collisions. *J. Phys. G* **2016**, *43*, 125102.

18. Lao, H.-L.; Liu, F.-H.; Li, B.-C.; Duan, M.-Y. Kinetic freeze-out temperatures in central and peripheral collisions: Which one is larger? *Nucl. Sci. Tech.* **2018**, *29*, 82.

19. Andronic, A. An overview of the experimental study of quark-gluon matter in high-energy nucleus-nucleus collisions. *Int. J. Mod. Phys. A* **2014**, *29*,1430047.

20. Abelev, B.; ALICE Collaboration. Pion, kaon, and proton production in central Pb–Pb collisions at $\sqrt{s_{NN}} = $ 2.76 TeV. *Phys. Rev. Lett.* **2012**, *109*, 252301.

21. Zhang, S.; Ma, Y.G.; Chen, J.H.; Zhong, C. Production of kaon and Λ in nucleus-nucleus collisions at ultrarelativistic energy from a blast-wave model. *Adv. High Energy Phys.* **2015**, *2015*, 460590.

22. Das, S. Identified particle production and freeze-out properties in heavy-ion collisions at RHIC beam energy scan program. In *EPJ Web of Conferences*; EDP Sciences: Jules, France, 2015; Volume 90, p. 08007.

23. Das, S.; STAR Collaboration. Centrality dependence of freeze-out parameters from the beam energy scan at STAR. *Nucl. Phys. A* **2013**, *904–905*, 891c–894c.

24. Abgrall, N.; NA61/SHINE Collaboration. Measurement of negatively charged pion spectra in inelastic p+p interactions at $p_{lab} = $ 20, 31, 40, 80 and 158 GeV/c. *Eur. Phys. J. C* **2014**, *74*, 2794.

25. Adare, A.; PHENIX Collaboration. Identified charged hadron production in $p + p$ collisions at $\sqrt{s} = 200$ and 62.4 GeV. *Phys. Rev. C* **2011**, *83*, 064903.

26. Aamodt, K.; ALICE Collaboration. Production of pions, kaons and protons in pp collisions at $\sqrt{s} = 900$ GeV with ALICE at the LHC. *Eur. Phys. J. C* **2011**, *71*, 1655.

27. Chatrchyan, S.; CMS Collaboration. Study of the inclusive production of charged pions, kaons, and protons in pp collisions at $\sqrt{s} = 0.9$, 2.76, and 7 TeV. *Eur. Phys. J. C* **2012**, *72*, 2164.

28. Sirunyan, A.M.; CMS Collaboration. Measurement of charged pion, kaon, and proton production in proton-proton collisions at $\sqrt{s} = 13$ TeV. *Phys. Rev. D* **2017**, *96*, 112003.

29. Petrovici, M.; Andrei, C.; Berceanu, I.; Bercuci, A.; Herghelegiu, A.; Pop, A. Recent results and open questions on collective type phenomena from A-A to pp collisions. *AIP Conf. Proc.* **2015**, *1645*, 52.

30. Cleymans, J.; Worku, D. Relativistic thermodynamics: Transverse momentum distributions in high-energy physics. *Eur. Phys. J. A* **2012**, *48*, 160.

31. Zheng, H.; Zhu, L.L. Comparing the Tsallis distribution with and without tthermodynamical description in $p + p$ collisions. *Adv. High Energy Phys.* **2016**, *2016*, 9632126.

32. Odorico, R. Does a transverse energy trigger actually trigger on large-P_T jets? *Phys. Lett. B* **1982**, *118*, 151–154.

33. Arnison, G.; UA1 Collaboration. Transverse momentum spectra for charged particles at the CERN proton-antiproton collider. *Phys. Lett. B* **1982**, *118*, 167–172.

34. Mizoguchi, T.; Biyajima, M.; Suzuki, N. Analyses of whole transverse momentum distributions in $p\bar{p}$ and pp collisions by using a modified version of Hagedorn's formula. *Int. J. Mod. Phys. A* **2017**, *32*, 1750057.

35. Hagedorn, R. Multiplicities, p_T distributions and the expected hadron$\longrightarrow$quark-gluon phase transition. *Riv. Nuovo Cimento* **1983**, *6*, 1.

36. Abelev, B.; ALICE Collaboration. Production of $\Sigma(1385)^{\pm}$ and $\Xi(1530)^0$ in proton-proton collisions at $\sqrt{s} = 7$ TeV. *Eur. Phys. J. C* **2015**, *75*, 1.

37. Aamodt, K.; ALICE Collaboration. Transverse momentum spectra of charged particles in proton-proton collisions at $\sqrt{s} = 900$ GeV with ALICE at the LHC. *Phys. Lett. B* **2010**, *693*, 53–68.

38. De Falco, A.; ALICE Collaboration. Vector meson production in pp collisions at $\sqrt{s} = 7$ TeV, measured with the ALICE detector. *J. Phys. G* **2011**, *38*, 124083.

39. Abelev,B.; ALICE Collaboration. Light vector meson production in pp collisions at $\sqrt{s} = 7$ TeV. *Phys. Lett. B* **2012**, *710*, 557–568.

40. Abt, I.; HERA-B Collaboration. K^{*0} and ψ meson production in proton-nucleus interactions at $\sqrt{s} = 41.6$ GeV. *Eur. Phys. J. C* **2007**, *50*, 315–328.

41. Abelev, B.; ALICE Collaboration. Inclusive J/ψ production in pp collisions at $\sqrt{s} = 2.76$ TeV. *Phys. Lett. B* **2012**, 718, 295–306. and Erratum *Phys. Lett. B* **2015**, *748*, 472–473.

42. Lakomov, I.; ALICE Collaboration. Event activity dependence of inclusive J/ψ production in p-Pb collisions at $\sqrt{s_{NN}} = 5.02$ TeV with ALICE at the LHC. *Nucl. Phys. A* **2014**, *931*, 1179–1183.

43. Abelev, B.; ALICE Collaboration. Heavy flavour decay muon production at forward rapidity in proton-proton collisions at $\sqrt{s} = 7$ TeV. *Phys. Lett. B* **2012**, *708*, 265–275.

44. Aad, G.; ATLAS Collaboration. Charged-particle multiplicities in pp interactions at $\sqrt{s} = 900$ GeV with the ATLAS detector at the LHC. *Phys. Lett. B* **2010**, *688*, 21–42.

45. Aad, G.; ATLAS Collaboration. Charged-particle multiplicities in pp interactions measured with the ATLAS detector at the LHC. *New J. Phys.* **2011**, *13*, 053033.

46. Aad, G.; ATLAS Collaboration. Measurement of charged-particle spectra in Pb+Pb collisions at $\sqrt{s_{NN}} = 2.76$ TeV with the ATLAS detector at the LHC. *J. High Energy Phys.* **2015**, *2015*, 050.

47. Aad, G.; ATLAS Collaboration. Charged-particle distributions in $\sqrt{s} = 13$ TeV pp interactions measured with the ATLAS detector at the LHC. *Phys. Lett. B* **2016**, *758*, 67–88.

48. Aad, G.; ATLAS Collaboration. Charged-particle distributions in pp interactions at $\sqrt{s} = 8$ TeV measured with the ATLAS detector. *Eur. Phys. J. C* **2016**, *76*, 403.

49. Avdyushev, V.A. A new method for the statistical simulation of the virtual values of parameters in inverse orbital dynamics problems. *Sol. Syst. Res.* **2009**, *43*, 543.

50. Liu, F.-H.; Gao, Y.-Q., Wei, H.-R. On descriptions of particle transverse momentum spectra in high energy collisions. *Adv. High Energy Phys.* **2014**, *2014*, 293873.

51. Cleymans, J. The physics case for the $\sqrt{s_{NN}} \approx 10$ GeV energy region. In *Walter Greiner Memorial Volume*, Hess, P.O.; Ed.; World Scientiflc, Singapore, 2018.

52. Bjorken, J.D. Highly relativistic nucleus-nucleus collisions: The central rapidity region. *Phys. Rev. D* **1983**, *27*, 140–151.

53. Okamoto, K.; Nonaka, C. A new relativistic viscous hydrodynamics code and its application to the Kelvin-Helmholtz instability in high-energy heavy-ion collisions. *Eur. Phys. J. C* **2017**, *77*, 383.
54. Zhang, S.; Ma, Y.G.; Chen, J.H.; Zhong, C. Beam energy dependence of Hanbury-Brown-Twiss radii from a blast-wave model. *Adv. High Energy Phys.* **2016**, *2016*, 9414239.
55. Adamczyk, L.; STAR Collaboration. Bulk properties of the medium produced in relativistic heavy-ion collisions from the beam energy scan program. *Phys. Rev. C* **2017**, *96*, 044904.
56. Luo, X.F. Exploring the QCD phase structure with beam energy scan in heavy-ion collisions. *Nucl. Phys. A* **2016**, *956*, 75–82.
57. Chatterjee, S.; Das, S.; Kumar, L.; Mishra, D.; Mohanty, B.; Sahoo, R.; Sharma, N. Freeze-out parameters in heavy-ion collisions at AGS, SPS, RHIC, and LHC energies. *Adv. High Energy Phys.* **2015**, *2015*, 349013.
58. Acharya, S.; ALICE Collaboration. Multiplicity dependence of light-flavor hadron production in pp collisions at $\sqrt{s} = 7$ TeV. *Phys. Rev. C* **2019**, *99*, 024906.
59. Gutay, L.G.; Hirsch, A.S.; Pajares, C.; Scharenberg, R.P.; Srivastava, B.K. De-confinement in small systems: Clustering of color sources in high multiplicity $\bar{p}p$ collisions at $\sqrt{s} = 1.8$ TeV. *Int. J. Mod. Phys. E* **2015**, *24*, 1550101.
60. Hirsch, A.S.; Pajares, C.; Scharenberg, R.P.; Srivastava, B.K. De-confinement in high multiplicity proton-proton collisions at LHC energies. *arXiv* **2018**, arXiv:1803.02301 [hep-ph].
61. Sahoo, P.; De, S.; Tiwari, S.K.; Sahoo, R. Energy and centrality dependent study of deconfinement phase transition in a color string percolation approach at RHIC energies. *Eur. Phys. J. A* **2018**, *54*, 136.
62. Li, L.L.; Liu, F.-H. Energy dependent kinetic freeze-out temperature and transverse flow velocity in high energy collisions. *Eur. Phys. J. A* **2018**, *54*, 169.
63. Sarkisyan, E.K.G.; Sakharov, A.S. On similarities of bulk observables in nuclear and particle collisions. CERN-PH-TH-2004-213. *arXiv* **2004**, arXiv:hep-ph/0410324.
64. Sarkisyan, E.K.G.; Sakharov, A.S. Multihadron production features in different reactions. *AIP Conf. Proc.* **2006**, *828*, 35.
65. Back, B.B.; PHOBOS Collaboration. Centrality and energy dependence of charged-particle multiplicities in heavy ion collisions in the context of elementary reactions. *Phys. Rev. C* **2006**, *74*, 021902(R).
66. Lao, H.-L.; Liu, F.-H.; Li, B.-C.; Duan, M.-Y.; Lacey, R.A. Examining the model dependence of the determination of kinetic freeze-out temperature and transverse flow velocity in small collision system. *Nucl. Sci. Tech.* **2018**, *29*, 164.
67. Song, H.C.; Zhou, Y.; Gajdošová, K. Collective flow and hydrodynamics in large and small systems at the LHC. *Nucl. Sci. Tech.* **2017**, *28*, 99.
68. He, X.-W.; Wei, H.-R.; Liu, F.-H. Chemical potentials of light hadrons and quarks from yield ratios of negative to positive particles in high energy *pp* collisions. *J. Phys. G* **2019**, *46*, 025102.
69. Tsallis, C. Possible generalization of Boltzmann-Gibbs statistics. *J. Stat. Phys.* **1988**, *52*, 479–487.
70. Biró, T.S.; Purcsel, G.; Ürmössy,K. Non-extensive approach to quark matter. *Eur. Phys. J. A* **2009**, *40*, 325.
71. Sjöstrand, T. High-energy physics event generation with PYTHIA 5.7 and JETSET 7.4. *Comput. Phys. Commun.* **1994**, *82*, 74–90.
72. Sjöstrand, T.; Mrenna, S.; Skands, P.Z. A brief introduction to PYTHIA 8.1. *Comput. Phys. Commun.* **2008**, *178*, 852–867.
73. Skands, P.; Carrazza, S.; Rojo, J. Tuning PYTHIA 8.1: The Monash 2013 tune. *Eur. Phys. J. C* **2014**, *74*, 3024.
74. Sjöstrand, T.; Mrenna, S.; Skands, P. PYTHIA 6.4 physics and manual. *J. High Energy Phys.* **2006**, *2006(05)*, 026.
75. Trainor, T.A. Comparing the PYTHIA Monte Carlo to a two-component (soft + hard) model of hadron production in high-energy p-p collisions. *Int. J. Mod. Phys. E* **2019**, *28*, 1950023.
76. Tawfik, A.N.; Yassin, H.; Abo Elyazeed, E.R. On thermodynamic self-consistency of generic axiomatic-nonextensive statistics. *Chin. Phys. C* **2017**, *41*, 053107.
77. Tawfik, A.N. Lattice QCD thermodynamics and RHIC-BES particle production within generic nonextensive statistics. *Phys. Part. Nucl. Lett.* **2018**, *15*, 199–209.
78. Tawfik1, A.; Yassin, H.; Abo Elyazeed,E.R. Chemical freezeout parameters within generic nonextensive statistics. *Indian J. Phys.* **2018**, *92*, 1325–1335.
79. Tawfik, A.N. Baryon-to-pion ratios within generic (non)extensive statistics. *PoS* **2016**, *ICHEP2016*, 1153.

80. Sahu, D.; Tripathy, S.; Pradhan, G.S.; Sahoo, R. Role of event multiplicity on hadronic phase lifetime and QCD phase boundary in ultrarelativistic collisions at energies available at the BNL Relativistic Heavy Ion Collider and CERN Large Hadron Collider. *Phys. Rev. C* **2020**, *101*, 014902.

81. Reisdorf, W.; FOPI Collaboration. Systematics of pion emission in heavy ion collisions in the 1A GeV regime. *Nucl. Phys. A* **2007**, *781*, 459–508.

82. Mitchell, J.T.; STAR Collaboration. RHIC critical point search: Assessing STAR's capabilities. *PoS* **2007**, *CPOD2006*, 019.